ARTICLE

OPEN

Check for updates

Semi-empirical approach to assess externally-induced photoluminescence linewidth broadening of halide perovskite nanocrystals with particle-size distribution

Hyun Myung Jang [1,5✉], Song Hee Lee [1,5], Kyung Yeon Jang[2,5], Jinwoo Park[2] & Tae-Woo Lee [1,2,3,4✉]

Colloidal nanocrystals (NCs) can be used to prepare high-color-purity metal halide perovskites (MHPs) for light-emitting displays. However, the NCs have a finite particle-size distribution, which broadens the linewidth of photoluminescence spectra under strong quantum confinement, and thereby degrades the color purity of the MHPs. This paper presents a simple method to quantify this externally-introduced broadening of linewidth Γ_{SD} by combining experimental size-distribution histogram with size-dependent photoluminescence-wavelength (PL-λ) curve. We develop a semi-empirical method to estimate the other three contributions to the experimentally-measured full-width at half-maximum, Γ_{EXP}. Namely: the intrinsic linewidth Γ_{LO} caused by exciton-longitudinal optical (LO) phonon Fröhlich coupling; the inhomogeneous linewidth Γ_o caused by imperfections-related scattering, and the broadening Γ_{QC} due to the quantum-confinement effect. We show that Γ_{LO} of a nanocrystal decreases together with the particle size, disappearing at 1.6 nm radius. Finally, we show that Γ_{LO} is correlated with the degree of Fröhlich-polaron formation, hence proportional to the long-range LO-phonon-electron coupling.

[1] Research Institute of Advanced Materials (RIAM), Seoul National University, Seoul, Republic of Korea. [2] Department of Materials Science and Engineering, Seoul National University, Seoul, Republic of Korea. [3] School of Chemical and Biological Engineering, Institute of Engineering Research, Soft Foundry, Seoul National University, Seoul, Republic of Korea. [4] SN Display Co. Ltd., Seoul, Republic of Korea. [5] These authors contributed equally: Hyun Myung Jang, Song Hee Lee, Kyung Yeon Jang. ✉email: jang0227@snu.ac.kr; twlees@snu.ac.kr

Metal halide perovskites (MHPs) have spectral tunability that covers ultraviolet to near-infrared wavelengths, high color purity, and low production cost, and are therefore possible next-generation luminescent materials for light-emitting diode (LED) displays[1–5]. The high color purity is a consequence of narrow emission linewidths (full-width at half-maximum (FWHM) ≤20 nm), and offers a wide color gamut over 140% of the National Television Standard Committee (NTSC) color standard. These attributes surpass the characteristics of organic emitters (FWHM >40 nm, color gamut <100% NTSC) and inorganic quantum dot (QD) emitters (FWHM ≈30–40 nm, color gamut ≈120% NTSC)[6].

Early perovskite LEDs achieved bright electroluminescence by using bulk polycrystalline films[2,5]. Subsequent perovskite LED technology progressed remarkably by using small nanograins[5], low-dimensionality layered crystals[7,8], and colloidal perovskite nanocrystals (PNCs)[9–11]. These approaches boost the quantum-confinement effect by reducing the grain or particle size, and strengthen the excitonic radiative recombination, and thereby increase the photoluminescence quantum efficiency (PLQE)[6,12,13]. The use of colloidal PNCs is an effective strategy to increase the PLQEs of MHP crystals[14–17]. This approach uses organic ligands[18,19], which limit growth of MHP crystals and stabilizes them to increase their dispersion stability in solution. MHPs have low exciton-binding energy, so the restriction of PNC size by ligands can overcome exciton dissociation[5,14]. Moreover, the MHP crystallization process ends in a solution state, which is weakly influenced by the environment, so colloidal PNCs can be reproducibly coated on a variety of substrates[20–23].

Both intrinsic and extrinsic factors can affect color purity by broadening the linewidth of the photoluminescence (PL) spectrum $\Gamma(T)$ at temperature T. For most photoluminescent semiconductors, these factors are divided into four terms[24–26]: $\Gamma(T) = \Gamma_o + \Gamma_{ac}(T) + \Gamma_{LO}(T) + \Gamma_{imp}$, where Γ_o denotes inhomogeneous line broadening caused by disorder and imperfections-related scattering, and is independent of temperature. $\Gamma_{ac}(T)$ and $\Gamma_{LO}(T)$ designate homogeneous line broadening, which arise from phonon scatterings and are dependent on temperature. $\Gamma_{ac}(T) = \gamma_{ac}T$, where γ_{ac} is the coupling strength of acoustic phonon and charge carriers. $\Gamma_{LO}(T) = \gamma_{LO}N_{LO}(T)$, where γ_{LO} is the coupling strength of longitudinal optical (LO) phonon and charge carriers, and $N_{LO}(T) = 1/\{e^{\hbar\omega_{LO}/k_BT} - 1\}$ represents the Bose-Einstein distribution function where $\hbar\omega_{LO}$ is

the energy of LO phonons. Γ_{imp} phenomenologically accounts for inhomogeneous scattering from ionized impurities.

A systematic study[27] of bulk polycrystalline films of hybrid MHPs MAPbBr$_3$, MAPbI$_3$, FAPbBr$_3$, and FAPbI$_3$ used the Bose-Einstein distribution function to fit the temperature-dependent FWHM of the PL peak, and thereby demonstrated that linewidth broadening in them at room temperature is primarily caused by long-range Fröhlich coupling between exciton carriers and LO phonons, with scattering $\Gamma_{ac}(T)$ from acoustic phonons and Γ_{imp} from impurities being minor components[27,28]. Thus, the net broadening factor can be expressed as $\Gamma_{net}(T) = \Gamma_{LO}(T) + \Gamma_o$. In their subsequent analysis, however, the temperature-independent imperfections-related scattering Γ_o term was implicitly absorbed in $\Gamma_{LO}(T)$ term[27,28]. The FWHM of the room-temperature steady-state spectrum of polycrystalline MAPbBr$_3$ film is $\Gamma(\lambda) = 23.4$ nm at $\lambda = 538$ nm (equivalent to $\Gamma(\hbar\omega) = 100.3$ meV), which slightly exceeds the high color-purity standard of FWHM ≤ 20 nm. Herein, $\Gamma(\lambda)$ denotes the FWHM of the PL-λ spectrum in which the PL intensity is plotted as function of the PL wavelength, whereas $\Gamma(\hbar\omega)$ denotes the FWHM of the PL-$\hbar\omega$ spectrum in which the PL intensity is plotted as function of the PL energy ($\hbar\omega$).

In a system of colloidal PNCs that show extraordinarily high PLQEs, the mechanism of the PL linewidth broadening seems to be more complicated than in bulk polycrystalline films due to an additional external factor that arises from the particle-size distribution. If colloidal PNCs are not strictly mono-disperse, an additional broadening mechanism is inevitably introduced because each NC shows a characteristic PL wavelength (PL-λ) associated with its own size, so a finite size distribution inevitably leads to a finite linewidth in the PL peak. In addition to this external broadening Γ_{SD} due to the size distribution, one should also consider linewidth broadening Γ_{QC} due to the quantum-confinement effect, especially for the particle whose radius is smaller than the exciton Bohr radius a_B[29]. Thus, the net FWHM in the PL-λ spectrum of colloidal PNCs at a fixed temperature (e.g., 300 K) can be written as

$$\Gamma_{net}(\lambda) = \Gamma_{LO}(\lambda) + \Gamma_o(\lambda) + \Gamma_{SD}(\lambda) + \Gamma_{QC}(\lambda), \quad (1)$$

where λ inside the parenthesis of each broadening term denotes the broadening contribution to the PL-λ spectrum. $\Gamma_{net}(\lambda)$ can be directly obtained from the observed broadening $\Gamma_{EXP}(\lambda)$ of the experimental PL-λ spectrum [i.e., $\Gamma_{net}(\lambda) = \Gamma_{EXP}(\lambda)$] and $\Gamma_{SD}(\lambda)$ denotes the externally-introduced FWHM that is caused

---

Table 1 Three nominal contributions to the size-dependent experimental linewidth of MAPbBr$_3$ CNCs, expressed in nm value.

D_p (nm)	R_p (nm)	λ_p (nm)	$\Gamma_{EXP}(\lambda)$ (nm)	$\Gamma_{SD}^{ext}(\lambda)$ (nm)	$\Gamma_{QC}(\lambda)$ (nm)	$\Gamma_{LO}^{ext}(\lambda)$ (nm)	ω_p ($\times 10^{15}s^{-1}$)	$\Gamma_{EXP}(\omega)$ ($\times 10^{15}s^{-1}$)
2.7	1.35	475	35.9	35	1.9	-1.0	3.966	0.293
3.2	1.6	498	33.7	32	1.7	0	3.783	0.256
5.0	2.5	514	28.9	18.5	1.1	9.3	3.665	0.206
6.0	3.0	518	26.4	14.5	0.9	11.0	3.637	0.185
7.5	3.75	522	22.2	6.0	0.8	15.4	3.609	0.154
8.7	4.35	523	22.3	5.4	0.7	16.2	3.602	0.154
9.9	4.95	524	23.4	4.5	0.6	18.3	3.595	0.161
19.5	9.75	525.1	23.5	2.2	0.3	21.0	3.587	0.161
22.5	11.25	526.0	24.7	2.2	0.3	22.2	3.582	0.168
23.7	11.85	526.2	25.5	2.2	0.2	23.1	3.580	0.174
27.5	13.75	527.0	25.5	---	---	---	3.575	0.173
	$(= R_c)$	$(= \lambda_c)$						

*The size-dependent three distinct linewidths are expressed in units of nm, which is in accordance with Eq. (3): $\Gamma_{EXP}(\lambda) \equiv \Gamma_{LO}^{ext}(\lambda) + \Gamma_{QC}(\lambda) + \Gamma_{SD}^{ext}(\lambda)$, where ′$\lambda$′ inside each parenthesis emphasizes that the corresponding PL spectrum is plotted as a function of the PL wavelength (λ).

*$\Gamma_{LO}^{ext}(\lambda)$ in Table 2 designates an extracted $\Gamma_{LO}(\lambda)$ value which is obtained using Eq. (3) and the following three contributions: (i) the size-dependent experimental $\Gamma_{EXP}(\lambda)$ value obtained from the corresponding PL-λ spectrum, (ii) the theoretically computed $\Gamma_{QC}(\lambda)$ value, and (iii) the experimentally extracted $\Gamma_{SD}^{ext}(\lambda)$ value. We can readily obtain the following relation between $\Gamma_{LO}^{ext}(\lambda)$ and $\Gamma_{LO}(R)$, where $\Gamma_{LO}(R)$ denotes the size-dependent linewidth solely caused by the exciton-LO phonon coupling (Γ_{LO}): $\Gamma_{LO}^{ext}(\lambda) = \Gamma_{LO}(R) + (\Gamma_o - \Delta_R)$ (Methods for details).

*We semi-empirically found that $\Gamma_{LO}^{ext}(\lambda) = \Gamma_{LO}(R)$ because $\Gamma_o = \Delta_R$ for $R \leq 4.95$ nm and $\Gamma_{LO}^{ext}(\lambda) = \Gamma_{LO}(bg) + (\Gamma_o - \Delta_R)$ for $R \geq 4.95$ nm where $\Gamma_{LO}(bg)$ denotes the Γ_{LO} value that corresponds to the bulk grains (18.3 nm for MAPbBr$_3$). Γ_{LO} for sufficiently coarsened grains in a polycrystalline film probably meets this requirement that $\Gamma_{LO} = \Gamma_{LO}(bg)$.

exclusively by the size distribution (Table 1). According to Eq. (1), the FWHM in the photoluminescence angular-frequency spectrum PL-ω can be written as $\Gamma_{net}(\omega) = \Gamma_{LO}(\omega) + \Gamma_o(\omega) + \Gamma_{SD}(\omega) + \Gamma_{QC}(\omega)$. A QD is a semiconductor nanoparticle that has a diameter less than its Bohr diameter $D_B(= 2a_B)$ and thus shows a strong quantum-confinement effect[29]. Hereafter, when the corresponding particle has $R < R_c$, which is the critical size for the onset of the PL blue shift (i.e., the incipient size for weak quantum confinement), we will refer to the particle as a confined nanocrystal (CNC). In an MAPbBr$_3$ CNC, we found that $R_c = 13.75$ nm from the size-dependent experimental PL-λ curve (Results and discussion).

Two additional broadening terms, Γ_{SD} and Γ_{QC}, are thus introduced in colloidally dispersed CNCs, as compared with bulk polycrystalline films[27]. The linewidth broadening due to these two terms is pronounced at small CNC sizes, which possibly deteriorates the ultrahigh color purity of MHPs. Therefore, it is of significance (i) to estimate the CNC-size-dependent contribution of these two broadening terms and (ii) to consequently find a suitable modal radius for maintaining both high color purity and high PLQE of colloidal PNCs (perovskite nanocrystals). For these purposes, we developed a simple method to extract Γ_{SD} at a given modal size by combining the experimental size-distribution histogram with the size-dependent PL-λ curve. We subsequently developed a semi-empirical method to estimate the other three contributions to the experimentally-measured FWHM, namely, Γ_{LO}, Γ_{QC}, and Γ_o. We show that Γ_{LO} of MAPbBr$_3$ disappears at the CNC radius $R = 1.60$ nm. The net FWHM $\Gamma_{net}(\lambda)$ obtained from the experimental PL-λ spectrum effectively remains at a constant plateau value (~ 23 nm) down to $R \approx 4.5$ nm, then rapidly increases as R decreases further. This result indicates that to maintain ultrahigh color purity of MHPs with high PLQEs, colloidal PNCs should have the modal radius (R_p) not less than ~ 4.5 nm. See Supplementary Table 1 for definition or explanation of various mathematical symbols used in the present study.

Results and discussion

Externally-introduced linewidth broadening due to CNC-size distribution
First, we will illustrate graphically that for a colloidal dispersion having a given CNC-size distribution, characteristic size-dependent variation of the PL wavelength λ does greatly alter the shape of the resulting PL-λ spectrum by considering two distinct types of the PL-λ vs. size (R) curve. There exists a unique 1:1 correspondence between the modal CNC size R_p and the corresponding PL wavelength (Methods). Thus, the CNC-size distribution $g(R)$ inevitably produces a finite linewidth $\Gamma_{SD} = \Delta\lambda'_{1/2} + \Delta\lambda_{1/2}$, where $\Delta\lambda'_{1/2}$ and $\Delta\lambda_{1/2}$ are respectively the half-widths at half-maximum on the short-λ and long-λ sides in the PL-λ spectrum $f(\lambda)$ (Fig. 1a, b). A linear variation in λ across R_p (Fig. 1c) and a nonlinear variation in λ across R_p (Fig. 1d) would lead to a slightly asymmetric $f(\lambda)$ spectrum with a $\Delta\lambda'_{1/2} > \Delta\lambda_{1/2}$ (Fig. 1e) and an asymmetric $f(\lambda)$ spectrum but with $\Delta\lambda_{1/2} < \Delta\lambda'_{1/2}$ (Fig. 1f), respectively. The slightly asymmetric $f(\lambda)$ in Fig. 1e occurs because $g(R)$ is a slightly asymmetric. This analysis predicts the absence of linewidth broadening in the PL-λ spectrum (i.e., $\Gamma_{SD}(\lambda) = 0$) if all CNCs have identical size (i.e., $\Delta R = 0$). However, it should be noted that $f(\lambda)$ schematically illustrates a hypothetical PL-λ spectrum that would be caused exclusively by the CNC-size distribution (Fig. 1e, f).

In contrast, a PL-λ spectrum caused by the intrinsic PL broadening Γ_{LO} should be Lorentzian in the absence of extrinsic broadening Γ_{SD} (Fig. 1g), where Γ_o is implicitly included in Γ_{LO} for convenience[27]. Then, the net linewidth in the real PL-λ spectrum is

obtained by (i) by shifting the intrinsic Lorentzian Γ_{LO} spectrum to the short-λ side by $\Delta\lambda'_{1/2}$ and to the long-λ side by $\Delta\lambda_{1/2}$ and (ii) adding $\frac{1}{2}\Gamma_{LO}$ to each of these two shifts caused by the CNC-size distribution (Fig. 1g); i.e., if Γ_{QC} is negligible, then $\Gamma_{net} = (\frac{1}{2}\Gamma_{LO} + \Delta\lambda'_{1/2}) + (\Delta\lambda_{1/2} + \frac{1}{2}\Gamma_{LO}) = \Gamma_{LO} + (\Delta\lambda'_{1/2} + \Delta\lambda_{1/2}) = \Gamma_{LO} + \Gamma_{SD}$.

The size distribution of MAPbBr$_3$ CNCs affects their PL spectrum and associated properties (Fig. 2). As the CNC size decreases, the peak wavelength λ_p gradually decreases in the normalized PL-λ spectrum (Fig. 2a), and the asymmetry of the PL spectrum tends to increase. The spectral asymmetry is very pronounced when the modal diameter $D_p (2R_p) = 2.7$ nm. PL-λ decreases slowly and linearly with decreasing D_p down to ~ 9 nm but decreases rapidly below this critical size, showing a pronounced PL blue shift beginning at ~ 9 nm (Fig. 2b). It can be shown theoretically that there exists a unique 1:1 correspondence between the particle size and the PL wavelength with an increasing tendency of the PL blue shift (moves towards a shorter λ_p) as R_p decreases (Methods). The critical size for the pronounced PL blue shift is close to the exciton Bohr diameter $D_B(= 2a_B)$ which is reported between 8.76 nm (ref. [30]) and 10 nm (ref. [29]) for MAPbBr$_3$. This result suggests that the strong quantum confinement (i.e., noticeable degree of the PL blue shift) begins to occur when the modal CNC diameter (radius) is reduced to its $D_B(a_B)$.

The FWHM of the PL-λ spectrum is plotted as a function of the modal diameter of MAPbBr$_3$ CNCs (Fig. 2c). According to the normalized PL-ω spectra (Fig. 2d), the modal frequency ω_p gradually moves towards the onset frequency $\omega_p = 3.575 \times 10^{15}$ s^{-1} of the PL blue shift as the CNC size increases. Unlike other PL-ω spectra, the PL-ω spectrum at $D_p = 2.7$ nm is highly asymmetric with (i) a strong skew toward the low-ω side and (ii) a long tail in the low-ω side of the peak frequency ω_p. The main reason behind this anomalous non-Lorentzian behavior will be analyzed theoretically in other section.

Extraction of size-dependent Γ_{SD}
Transmission-electron microscopy (TEM) images of colloidally dispersed CNCs were captured at various modal diameters of MAPbBr$_3$ (Fig. 3a), and their modal-diameter-dependent size-distribution histograms were compiled. The degree of size distribution (i.e., polydispersity) in the synthesized MAPbBr$_3$ CNCs decreased prominently as D_p decreased; the polydispersity in size, i.e., ΔR in $g(R)$ (Fig. 1a) was as small as ~ 1 nm at $D_p = 2.7$ nm (Supplementary Table 2, Supplementary Fig. 1).

The $f(\lambda)$ spectrum (Fig. 1e, f) can be extracted in a simple manner by combining the experimental size-distribution histogram with the size-dependent PL-λ curve (Fig. 3b), where $f(\lambda)$ again denotes a hypothetical PL-λ spectrum that is exclusively caused by the CNC-size distribution described by $g(R)$. $\Gamma_{SD}(\lambda)$ can be easily extracted from the difference between the two points on the horizontal line that intersects the extracted $f(\lambda)$ curve at $f(\lambda) = 1/2$ (Supplementary Table 2). For a CNC assembly with $D_p = 7.5$ nm as an illustrative example, $\Gamma^{ext}_{SD}(\lambda) = 523.6$ nm $- 517.6$ nm $= 6.0$ nm (Fig. 3b), where $\Gamma^{ext}_{SD}(\lambda)$ denotes $\Gamma_{SD}(\lambda)$ extracted from the size-dependent PL-λ curve combined with the experimental size-distribution histogram (Supplementary Fig. 1). In this way, we extracted $f(\lambda)$ spectra for nine modal diameters (Fig. 3c and Supplementary Fig. 2); $\Gamma^{ext}_{SD}(\lambda)$ decreased dramatically as D_p increased and tended toward an asymptote of 2.2 nm at $D_p \geq 19.5$ nm. The main reason for obtaining a narrow $f(\lambda)$ spectrum (i.e., small Γ_{SD}) at large modal diameters is that $d\lambda/dD$ decreases significantly as D_p increases (Fig. 2b) although the
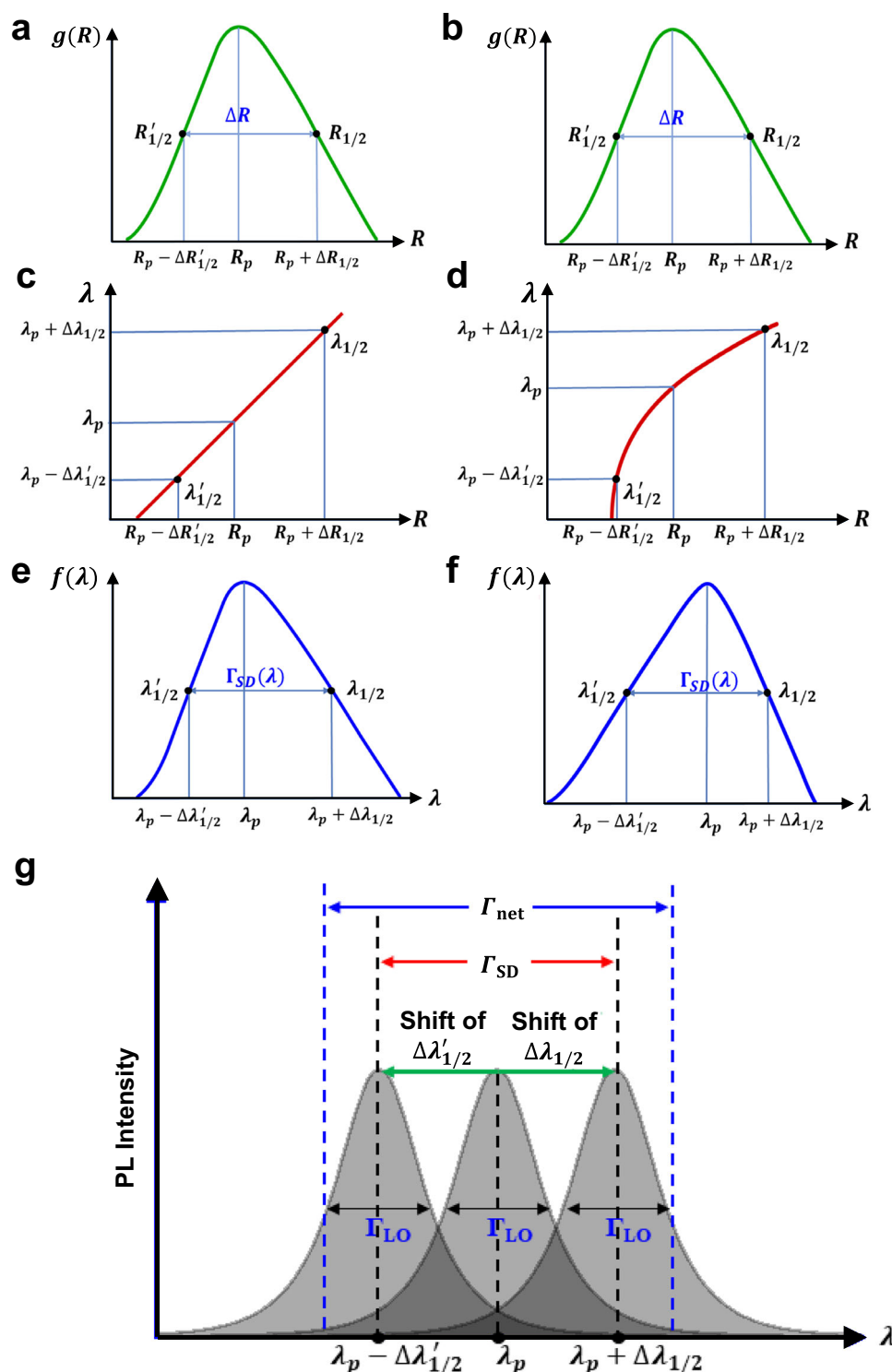
Fig. 1 Linewidth broadening arising from the polydispersity in CNC-size distribution $g(R)$. a, **b** CNC-size distribution $g(R)$ depends on the size.
c Hypothetical linear variation and (**d**) nonlinear variation in the PL wavelength λ across the modal CNC (confined nanocrystal) size would produce (**e**) a slightly asymmetric $f(\lambda)$ spectrum that is skewed toward the long-λ side of the modal (peak) λ_p, and (**f**) a spectrum with a slight skew toward the short-λ side of λ_p for the same CNC-size distribution $g(R)$. **g** Schematic diagram that graphically illustrates the relation, $\Gamma_{net} \approx \Gamma_{LO} + \Gamma_{SD}$. Herein, we ignore Γ_{QC} and Γ_o to simplify our discussion at a conceptual level.

polydispersity in the CNC-size distribution increases noticeably as D_p increases (Fig. 3a). This results in narrow $f(\lambda)$ spectra that have a common linewidth of ~ 2.2 nm.

However, the correct Γ_{SD} value for colloidal CNCs having a finite degree of the size distribution is substantially different

from Γ_{SD}^{ext} due to a nonlinearity in the size-dependent PL-λ curve. According to our analysis described in Methods, the extracted value Γ_{SD}^{ext} is significantly overestimated as compared with the correct Γ_{SD} value with the degree of overestimate designated by Δ_R. Accordingly, we empirically establish the
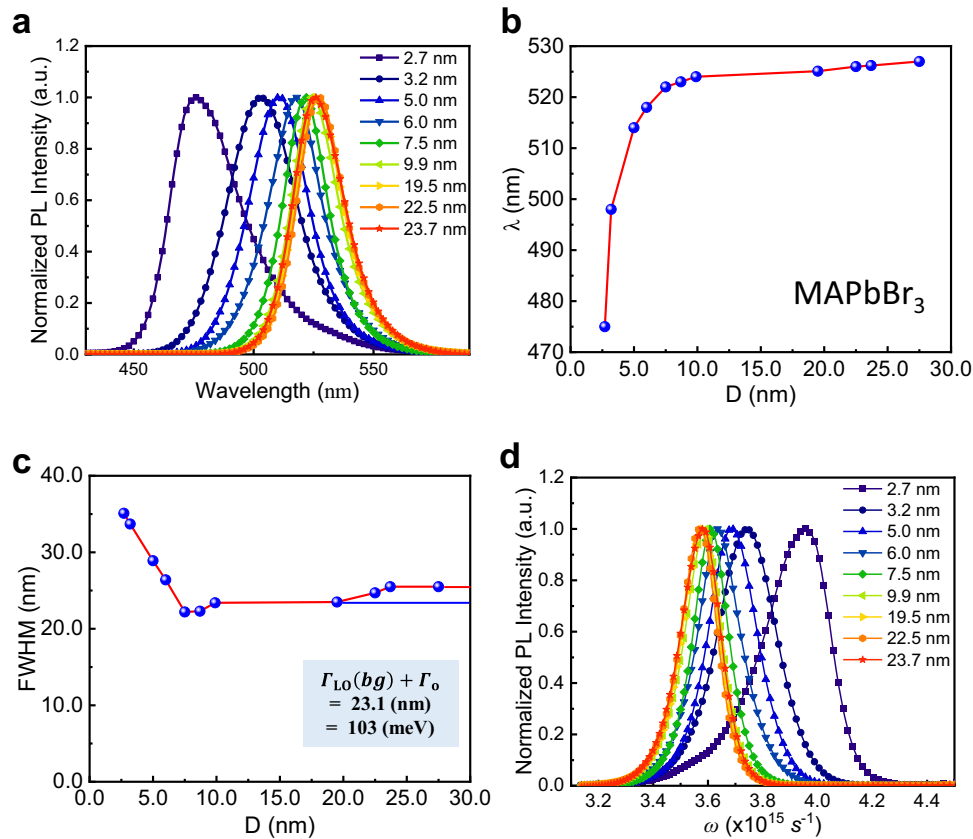
Fig. 2 Size-dependent PL spectra and associated properties of MAPbBr₃ CNCs. a Normalized PL intensity *vs.* PL wavelength (i.e., PL-λ spectrum) of MAPbBr₃ CNCs (confined nanocrystals) having various modal diameters. **b** Experimentally measured PL wavelength λ of MAPbBr₃ CNCs plotted as a function of the modal CNC diameter obtained from the corresponding size-distribution histogram. **c** Experimentally obtained FWHM (full-width at half-maximum) Γ_{EXP} *vs.* modal diameter of MAPbBr₃ CNCs. This size-dependent experimental FWHM was obtained directly from the corresponding PL-λ spectrum. It can be shown that the difference between the red horizontal Γ_{EXP} line and the blue horizontal line comprises the two independent contributions: $\Delta\Gamma_{SD} + \Delta\Gamma_{QC} = 2.1 - 0.1 = 2.0$(nm), where $\Delta\Gamma_{QC}$ represents the difference in Γ_{QC} between the CNCs with $D_p = 23.7$ nm and the CNCs with $D_p = 19.5$ nm namely, $\Gamma_{QC} = (0.2 - 0.3)$ nm, because $\Delta\Gamma_{LO} = 18.3 - 18.3 = 0$. **d** Normalized PL intensity *vs.* PL frequency (*i.e.*, PL-ω spectrum) of MAPbBr₃ CNCs having various modal diameters.

following equation:

$$\Gamma_{SD}^{ext}(\lambda) = \Gamma_{SD}(\lambda) + \Delta_R \qquad (2)$$

It can be shown that $\Delta_R = 0$ (i.e., $\Gamma_{SD}^{ext} = \Gamma_{SD}$) if the following two requirements are simultaneously satisfied: (i) a symmetric size distribution $g(R)$ with respect to the modal radius R_p and (ii) a linearity in the size-dependent PL-λ curve.

**Size-dependent three nominal contributions to net linewidth.** The three distinct contributions to the experimental net linewidth, $\Gamma_{EXP}(\lambda)$, vary as the CNC radius varies (Fig. 4a). Here, the three nominal contributions are $\Gamma_{LO}^{ext}(\lambda), \Gamma_{QC}(\lambda)$, and $\Gamma_{SD}^{ext}(\lambda)$. $\Gamma_{LO}^{ext}(\lambda)$ in Fig. 4a is not the true intrinsic $\Gamma_{LO}(\lambda)$ value but designates an indirect estimate obtained from (i) the experimental $\Gamma_{EXP}(\lambda)$, (ii) the extracted $\Gamma_{SD}^{ext}(\lambda)$, and (iii) the theoretically computed $\Gamma_{QC}(\lambda)$ using the following nominal definition:

$$\Gamma_{EXP}(\lambda) \equiv \Gamma_{LO}^{ext}(\lambda) + \Gamma_{QC}(\lambda) + \Gamma_{SD}^{ext}(\lambda) \qquad (3)$$

where $\Gamma_{LO}^{ext}(\lambda)$ absorbs Γ_o term in Eq. (1). The main reason for absorbing Γ_o term into $\Gamma_{LO}^{ext}(\lambda)$ is that we are not able to separately evaluate $\Gamma_{LO}(\lambda)$ and $\Gamma_o(\lambda)$ at this stage. It can be shown readily that $\Gamma_{LO}^{ext} = \Gamma_{LO} + (\Gamma_o - \Delta_R)$ (Methods). This signifies that the nominal Γ_{LO}^{ext} absorbs the Γ_o term[27] into Γ_{LO} but is corrected by the overestimate Δ_R made in the experimental extraction of Γ_{SD}^{ext}.

As described in Methods, we estimated $\Gamma_{LO}(\lambda)$ and $\Gamma_o(\lambda)$ separately by comparing $\Gamma_{LO}^{ext}(R = 11.85$ nm) with $\Gamma_{LO}^{ext}(R = 4.95$ nm), where $\Gamma_{LO}^{ext}(R = 11.85$ nm) denotes the value of Γ_{LO}^{ext} at $R = 11.85$ nm. The semi-empirically estimated Γ_o is 4.8 nm in the PL-λ spectrum. In addition, we semi-empirically found that (i) $\Gamma_{LO}^{ext}(\lambda) = \Gamma_{LO}(\lambda) \equiv \Gamma_{LO}(R)$ for $R \leq 4.95$ nm, where $\Gamma_o \approx \Delta_R$ and (ii) $\Gamma_{LO}^{ext}(\lambda) = \Gamma_{LO}(bg) + (\Gamma_o - \Delta_R)$ for $R \geq 4.95$ nm. Herein, $\Gamma_{LO}(R)$ denotes the CNC-radius-dependent intrinsic linewidth solely caused by the exciton-LO phonon coupling (Γ_{LO}). $\Gamma_{LO}(R)$ is a rapidly decaying function of R varying from 18.3 nm to 0 nm as R decreases from 4.95 nm to 1.60 nm (Methods for details). On the other hand, $\Gamma_{LO}(bg)$ denotes the $\Gamma_{LO}(\lambda)$ value that corresponds to the bulk grains. It is estimated to be 18.3 nm for MAPbBr₃. Γ_{LO} for sufficiently coarsened grains in a polycrystalline film probably meets this requirement that $\Gamma_{LO}(\lambda) = \Gamma_{LO}(bg)$.

We computed the size-dependent overestimate Δ_R by using the following equation that can be obtained by combining Eq. (2) with Eq. (1): $\Delta_R = \{\Gamma_{LO} + \Gamma_o + \Gamma_{QC} + \Gamma_{SD}^{ext}\} - \Gamma_{EXP}$. In the case of MAPbBr₃ CNCs, Δ_R lies somewhere between 0 and 5.8 nm, approaching 0 as the modal radius increases. Semi-empirical calculations (Methods) indicate that Δ_R decreases noticeably with increasing radius beginning at $R = 4.95$ nm and becomes effectively 0 at $R = 11.85$ nm (Fig. 4b). Thus, $\Gamma_{SD}^{ext}(\lambda) \approx \Gamma_{SD}(\lambda)$ for $R \geq 11.85$ nm. Consequently, $\Gamma_{SD}^{ext}(\lambda)$ or $\Gamma_{SD}(\lambda)$ reaches a constant plateau value of 2.2 nm as the CNC size increases to
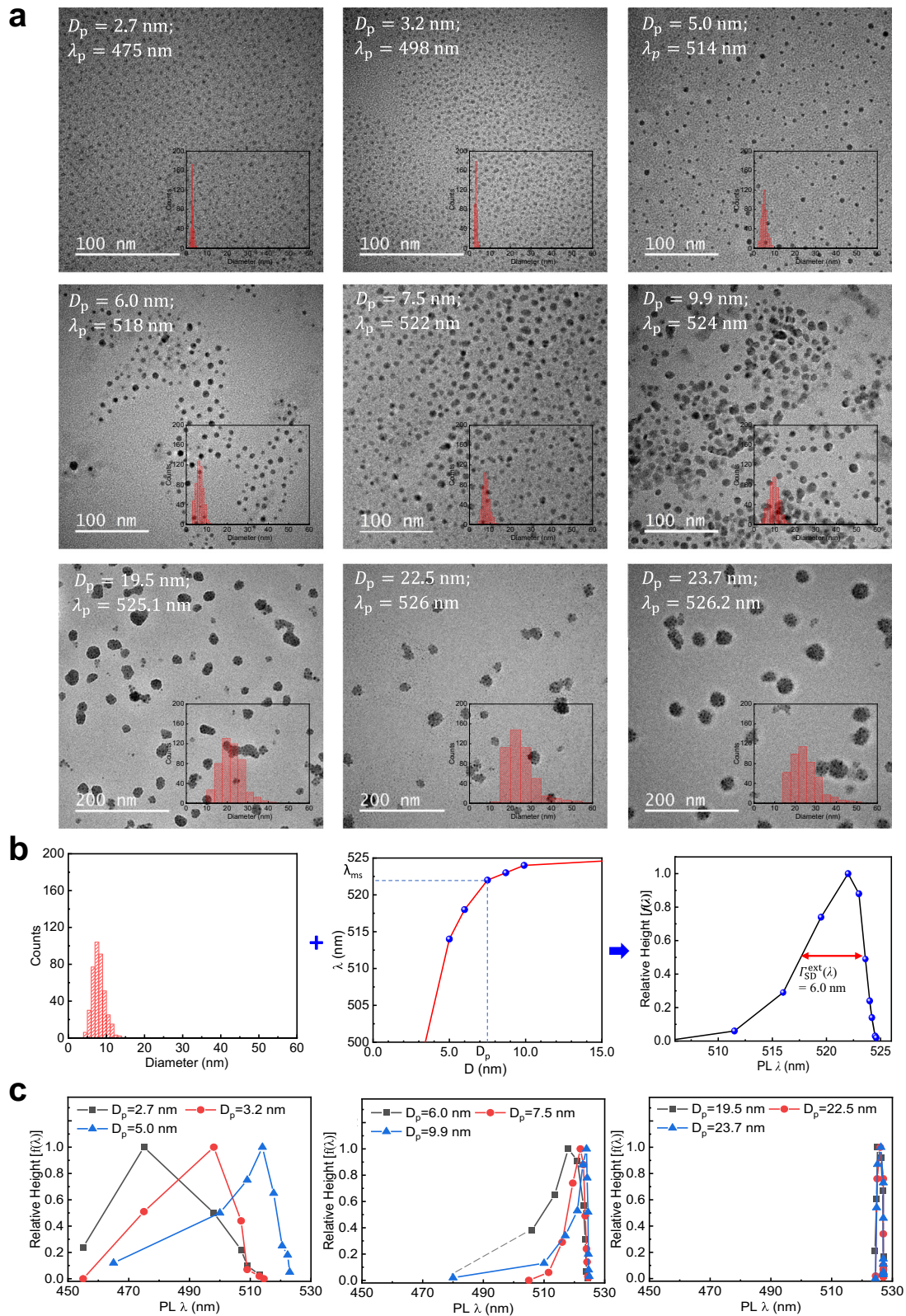
$R_c = 13.75$ nm (Fig. 4a), where R_c is the critical radius at which the PL blue shift begins (Table 1).

The quantum-confinement contribution to the linewidth broadening was calculated as[29] $\Gamma_{QC}(\lambda) = \frac{3\hbar\lambda_p}{\mu_o c R_p}\left(1 - \frac{3C_1'}{\pi^2}\right) = 0.544 \times 10^{-11}\left(\frac{\lambda_p}{R_p}\right)$, where λ_p denotes the PL wavelength that

corresponds to the modal (peak) radius R_p, and μ_o designates the effective mass of the exciton ($= 0.13m_o$ for MAPbBr$_3$)[30], where m_o denotes the free-electron mass (9.109×10^{-31} kg). C_1' is the modified effective Madelung constant for a spherical CNC, and it is modulated from $C_1 = 1.786$ by considering the dielectric-confinement effect[31] that arises from the surrounding low

Fig. 3 Size-dependent characteristics and a simple method of extracting PL-λ curve. a TEM images of the colloidally dispersed CNCs (confined nanocrystals) for various modal diameters (2.7 nm $\leq D_p \leq$ 23.7 nm) of MAPbBr$_3$ with the size-distribution histograms for various modal sizes. **b** Schematic diagrams that illustrate a simple method of extracting the $f(\lambda)$ curve and the associated FWHM (full-width at half-maximum) using the CNCs assembly with D_p = 7.5 nm as a standard example. The extracted $\Gamma_{SD}^{ext}(\lambda)$ is not the net FWHM of the experimental PL-λ curve but is the FWHM of hypothetical $f(\lambda)$ spectrum, which is caused exclusively by the CNC-size distribution under a nonlinear variation of the PL wavelength λ with the CNC size. **c** Extracted $f(\lambda)$ spectra of MAPbBr$_3$ CNCs *vs.* PL wavelength for nine different modal diameters between 2.7 nm and 23.7 nm. $f(\lambda)$ curve denotes the λ-dependent PL spectrum which would be exclusively caused by the CNC-size distribution, and thus is not the λ-dependent net experimental PL-λ spectrum. The extracted result indicates that $\Gamma_{SD}^{ext}(\lambda)$ decreases dramatically as modal size increases and tends toward an asymptote of 2.2 nm for $D_p \geq$ 19.5 nm.

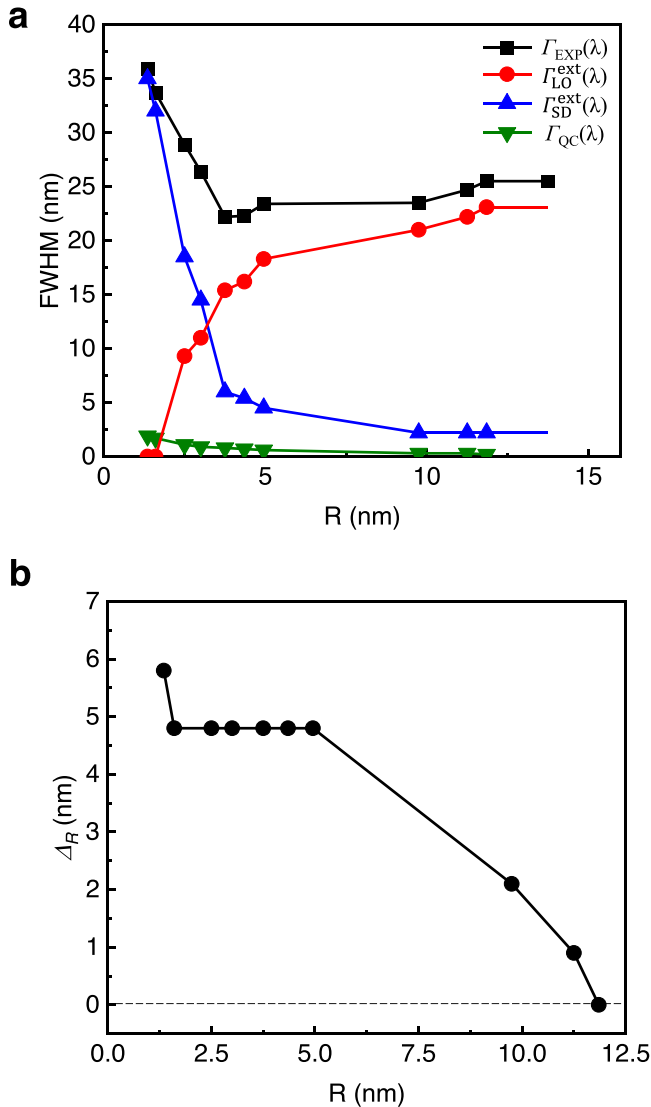**Fig. 4 Three nominal contributions to net linewidth. a** Three nominal contributions to the net experimental linewidth $\Gamma_{EXP}(\lambda)$ (black) of MAPbBr$_3$ vs. CNC (confined nanocrystals) radius. *λ* inside the parenthesis of each broadening term indicates that the corresponding PL intensity is displayed as a function of λ (not of ω). $\Gamma_{LO}^{ext}(\lambda)$ (red) designates an extracted $\Gamma_{LO}(\lambda)$ value which is obtained using Eq. (3) and the following three distinct contributions: (i) experimental $\Gamma_{EXP}(\lambda)$, (ii) theoretically computed $\Gamma_{QC}(\lambda)$ (green), and (iii) experimentally extracted $\Gamma_{SD}^{ext}(\lambda)$ (blue). We semi-empirically deduced that $\Gamma_{LO}^{ext}(\lambda)$ is equal to the correct intrinsic $\Gamma_{LO}(\lambda)$ for $R \leq 4.95$ nm. **b** Semi-empirically deduced size-dependent Δ_R over a wide range of the CNC radius. It shows a constant plateau behavior up to R = 4.95 nm and decays to zero at R = 11.85 nm A non-zero Δ_R indicates that there exists a certain degree of nonlinearity in the size-dependent PL wavelength for a CNC having the radius R.

dielectric-permittivity medium. The evaluated C_1' value is 1.39 for MAPbBr$_3$ CNCs dispersed in a toluene[29]. The three nominal contributions to Γ_{EXP}, namely, Γ_{LO}^{ext}, Γ_{QC}, and Γ_{SD}^{ext}, are listed in the unit of wavelength (nm) in Table 1 and in the unit of energy (meV) in Table 2.

Corrected four distinct contributions to net linewidth. The four corrected contributions to $\Gamma_{EXP}(\lambda)$ are plotted as a function of the CNC radius (Fig. 5a). The contribution of Γ_o to $\Gamma_{EXP}(\lambda)$ is constant and independent of the CNC radius. The semi-empirically estimated Γ_o is 4.8 nm in the PL-λ spectrum (Methods). It can be shown readily that 4.8 nm is equivalent to 21.4 meV in the PL-energy (i.e., PL-$\hbar\omega$) spectrum. This value is substantially smaller than $\sim$ 30 meV obtained by curve fitting of the temperature-dependent linewidth data of polycrystalline MAPbBr$_3$ film with the Bose-Einstein distribution function[27]. The difference of $\sim$ 8.6 meV (i.e., $30-21.4$) is due to structural disorders and imperfections presumably introduced during the film-forming processes that include annealing step at 100°C after spin coating[27].

The corrected $\Gamma_{SD}(\lambda)$ was evaluated using size-dependent Δ_R (Eq. 4b) and Eq. (2). $\Gamma_{SD}(\lambda)$ shows a rapid increase beginning at R = 4.95 nm. In contrast, $\Gamma_{LO}(\lambda)$ decreases rapidly with decreasing radius beginning at the same radius, 4.95 nm. However, $\Gamma_{LO}(\lambda)$ shows a constant plateau value of 18.3 nm beyond this particular size. The most prominent features of Fig. 5a are (i) the rapid decrease of $\Gamma_{LO}(\lambda)$ with decreasing CNC size, and (ii) the disappearance of $\Gamma_{LO}(\lambda)$ when the CNC radius decreases to 1.6 nm (i.e., D = 3.2 nm). Similar to the present finding, it was reported[32] that the long-range Fröhlich interaction decreased with a concomitant narrowing of linewidth in quasi-zero-dimensional ZnO CNCs (~4 nm in average size), as compared with unconfined bulk ZnO crystals. Phonons are long-range collective excitations of lattice vibrations, so this observation can be attributed to the reduced range of translational symmetry[32] in the collective excitations.

The R-dependent Γ_{LO} scales well with the reduced long-range Coulomb potential $\varphi_r(R)$ (Fig. 5b). Here, $\varphi_r(R)$ is defined as $\phi^{LR}(R)/\phi^{LR}(\infty)$, where $\phi^{LR}(R)$ is the long-range Coulomb interaction potential between the excess electron (or hole) and the ionic lattice in a CNC of radius R, which is considered to be the main driving force for the formation of the large Fröhlich polaron[33,34]. Here, $\Gamma_{LO}^{(1s)}$ emphasizes the exciton-LO phonon linewidth associated with the PL emission to the exciton's 1s ground state. The observed scaling between $\Gamma_{LO}(R)$ and $\varphi_r(R)$ indicates that the ratio $\Gamma_{LO}(R)/\varphi_r(R)$ is constant and independent of R over a wide range, and suggests a linear correlation between $\Gamma_{LO}(R)$ and $\phi^{LR}(R)$, where $\Gamma_{LO}(R)$ is used to emphasize the strongly R-dependent $\Gamma_{LO}(\lambda)$ for $R \leq 5.0$ nm in the PL-λ spectrum. Thus, $\Gamma_{LO}(R) = \Gamma_{LO}(R;\lambda)$. In the next section, we will clarify theoretically this proposition of the R-independent constant ratio.

Table 2 Three distinct contributions to the size-dependent experimental linewidth of MAPbBr$_3$ CNCs, expressed in meV value.

D_p (nm)	R_p (nm)	λ_p (nm)	ω_p ($\times 10^{15}$ s^{-1})	$\Gamma_{EXP}(\hbar\omega)$ (meV)	$\Gamma_{SD}^{ext}(\hbar\omega)$ (meV)	$\Gamma_{QC}(\hbar\omega)$ (meV)	$\Gamma_{LO}^{ext}(\hbar\omega)$ (meV)	$\Gamma_{EXP}(\omega)$ ($\times 10^{15}$ s^{-1})
2.7	1.35	475	3.966	197	192	10.4	—	0.293
3.2	1.6	498	3.783	169	160	8.5	0	0.256
5.0	2.5	514	3.665	136	87	5.2	44	0.206
6.0	3.0	518	3.637	122	67	4.2	51	0.185
7.5	3.75	522	3.609	101	27	3.6	70	0.154
8.7	4.35	523	3.602	100	24	3.2	73	0.154
9.9	4.95	524	3.595	106	20	2.7	83	0.161
19.5	9.75	525.1	3.587	105	10	1.4	94	0.161
22.5	11.25	526.0	3.582	111	10	1.3	100	0.168
23.7	11.85	526.2	3.580	114	10	0.9	103	0.174
27.5	13.75	527.0	3.575	114	—	—	—	0.173
($= R_c$)	($= \lambda_c$)	($= \omega_c$)						

* The size-dependent three distinct linewidths are expressed in units of energy ($\hbar\omega$) in Table 2. In contrast, the three linewidths are expressed in nm unit in Table 1.
* The following equations can interconvert the FWHMs between the PL-ω and PL-λ spectra: $\Gamma_{SD}(\omega) = \Gamma_{SD}(\hbar\omega)/\hbar = 2\pi c\Gamma_{SD}(1/\lambda) = 2\pi c\{\frac{1}{(\lambda_p - \frac{1}{2}\Gamma_{SD}(\lambda))} - \frac{1}{(\lambda_p + \frac{1}{2}\Gamma_{SD}(\lambda))}\} = \frac{2\pi c\Gamma_{SD}(\lambda)}{\{\lambda_p^2 - (\frac{1}{2}\Gamma_{SD}(\lambda))^2\}} \approx \frac{2\pi c\Gamma_{SD}(\lambda)}{\lambda_p^2}$, where

$\lambda_p^2 \gg (\frac{1}{2}\Gamma_{SD}(\lambda))^2$. Thus, we establish the following relation: $\Gamma_{SD}(\hbar\omega) = hc\,\Gamma_{SD}(\lambda)/\lambda_p^2$, where $\Gamma_{SD}(\lambda)$ represents the contribution of the CNC-size distribution to the net linewidth in the PL-λ spectrum (expressed in nm unit). Similarly, $\Gamma_{LO}(\hbar\omega)$ and $\Gamma_{QC}(\hbar\omega)$ are estimated using the following relations: $\Gamma_{LO}(\hbar\omega) = hc\,\Gamma_{LO}(\lambda)/\lambda_p^2$ and $\Gamma_{QC}(\hbar\omega) = hc\,\Gamma_{QC}(\lambda)/\lambda_p^2$.

Correlation of $\Gamma_{LO}(R)$ with the long-range Coulomb potential. The linear correlation between $\Gamma_{LO}(R)$ and $\phi^{LR}(R)$ for $R \leq 5.0$ nm further suggests that the Fröhlich-polaron radius might affect the variation of the PL linewidth. $\Gamma_{LO}(R)$ decreases rapidly when the CNC radius is smaller than a certain critical value $R_{rd} \approx 5.0$ nm (Fig. 5b). We therefore tested whether R_{rd} is correlated with the equilibrium polaron size. The following equation can be obtained for the radius r_p of the large Fröhlich polarons for a weak or moderate electron-LO phonon coupling[35]:

$$r_p^2 = \frac{2\hbar^2}{m_b(\hbar\omega_{LO})}\left(1 - \frac{\alpha}{6}\right), \quad (4)$$

where m_b is the effective band mass, which can be approximated by the effective reduced mass of exciton ($0.117 m_o$) and $\omega_{LO} = 167$ cm^{-1} for MAPbBr$_3$ (ref. [36]). The dimensionless Fröhlich coupling constant $\alpha \leq 2$ is a measure of the degree of the electron-LO or hole-LO phonon coupling that is responsible for the formation of large Fröhlich polarons ($\alpha = 1.69$ for MAPbBr$_3$)[36]. Plugging these values into Eq. (4) yields $r_p \approx 6.7$ nm. The experimental critical CNC radius for a rapid decrease in $\Gamma_{LO}(R)$ is ~ 5.0 nm ($\equiv R_{rd}$) (Fig. 5b) and is substantially smaller than the equilibrium polaron radius (6.7 nm). This result suggests that the PL linewidth tends to decrease rapidly when the large Fröhlich polaron is physically confined under the condition that $R_{rd} < r_p$. We will show subsequently that the decrease in $\Gamma_{LO}(R)$ with decreasing R is linearly correlated with the reduced driving force $\phi^{LR}(R)$ for the formation of large Fröhlich polarons.

Large Fröhlich polarons are formed by a long-range interaction between an electron and LO phonons[33,37]. Similarly, the PL linewidth broadening Γ_{LO} originates from the exciton-LO phonon coupling[24]. The strength of the electron-LO phonon coupling is expressed by the dimensionless Fröhlich coupling constant α (ref. [37]). α is proportional to the long-range Coulomb potential for a bulk state, $\phi^{LR}(R = \infty)$ (Supplementary Notes 1). $\phi^{LR}(\infty)$ in a bulk material is given by[34]

$$\phi^{LR}(\infty) = -\frac{e}{4\pi\varepsilon_o|r|}\left(\frac{1}{\varepsilon_{r(\infty)}} - \frac{1}{\varepsilon_{r(0)}}\right) \equiv -\frac{e}{4\pi\varepsilon_o\varepsilon_{r(\infty)}^{eff}|r|} < 0. \quad (5)$$

where $|r|$ is the distance between the excess electron (or hole) and the ionic lattice. ϕ^{LR} is the ensemble average of the long-range Coulomb potential operator $\widetilde{\phi}(r)$, and it is given by[33,37] $\widetilde{\phi}(r) =$

$-\frac{1}{e}\sum_q (V_q a_q^- e^{+iq\cdot r} + V_q^* a_q^+ e^{-iq\cdot r})$, where a_q^+ and a_q^-, respectively, are the creation and annihilation operators for the LO phonon with the wave vector $\mathbf{q}$ and energy $\hbar\omega_{LO}$. V_q denotes the Fourier component in the electron-LO phonon interaction Hamiltonian, and its magnitude $|V_q|$ is proportional to $\alpha^{1/2}$. Applying Eq. (5) to a dielectrically-confined CNC of radius R, and adopting the effective-action thickness approximation, we eventually obtain the following approximate expression of the Coulomb potential for a dielectrically-confined CNC of radius R (Supplementary Notes 1):

$$\phi^{LR}(R) = -\frac{e}{4\pi\varepsilon_o\varepsilon_r^Q|r|}\left[1 - \left\{\left(\frac{\varepsilon_r^Q}{\varepsilon_r^s}\right) - 1\right\}\left(\frac{L_{eff}}{R + L_{eff}}\right)\right], \quad (6)$$

where ε_r^Q designates the relative dielectric permittivity (hereafter, dielectric constant) of a CNC (or QD) core that is surrounded by a low-permittivity solvent having the dielectric constant ε_r^s, and L_{eff} denotes the effective-action thickness of the low-permittivity solvent layer. Thus, the (dimensionless) reduced long-range Coulomb potential is

$$\varphi_r(r) \equiv \frac{\phi^{LR}(R)}{\phi^{LR}(\infty)} = 1 - \left\{\left(\frac{\varepsilon_r^Q}{\varepsilon_r^s}\right) - 1\right\}\left(\frac{L_{eff}}{R + L_{eff}}\right). \quad (7)$$

The dielectric-confinement effect is negligible at $R = \infty$, so in obtaining Eq. (7), we implicitly used the asymptotic relation $\varepsilon_r^Q \to \varepsilon_{r(\infty)}^{eff}$ as the CNC size approaches its bulk value (i.e., as $R \to \infty$).

We have shown that this reduced long-range Coulomb potential can be expressed in terms of the dielectric-confinement effect on the exciton-LO phonon coupling contribution to the PL linewidth (Supplementary Notes 1). More explicitly, we have

$$\frac{\Gamma_{LO}^{(1s)}(R)}{\Gamma_{LO}^{(1s)}(\infty)} = \frac{\phi^{LR}(R)}{\phi^{LR}(\infty)} \equiv \varphi_r(R). \quad (8)$$

Equation (8) indicates that size-dependent PL linewidth $\Gamma_{LO}^{(1s)}(R)$ is proportional to the reduced long-range Coulomb potential $\varphi_r(R)$ because $\Gamma_{LO}^{(1s)}(\infty)$ is R-independent constant. This supports the scaling shown in Fig. 5b. In other words, the PL linewidth $\Gamma_{LO}^{(1s)}(R)$ is directly proportional to the long-range Coulomb potential $\phi^{LR}(R)$ associated with the electron-LO phonon coupling which is needed for the large Fröhlich-polaron formation[33,34]. Equation (8) also predicts that the PL linewidth caused by the exciton-LO phonon coupling reduces to zero when the driving force $\phi^{LR}(R)$ for the
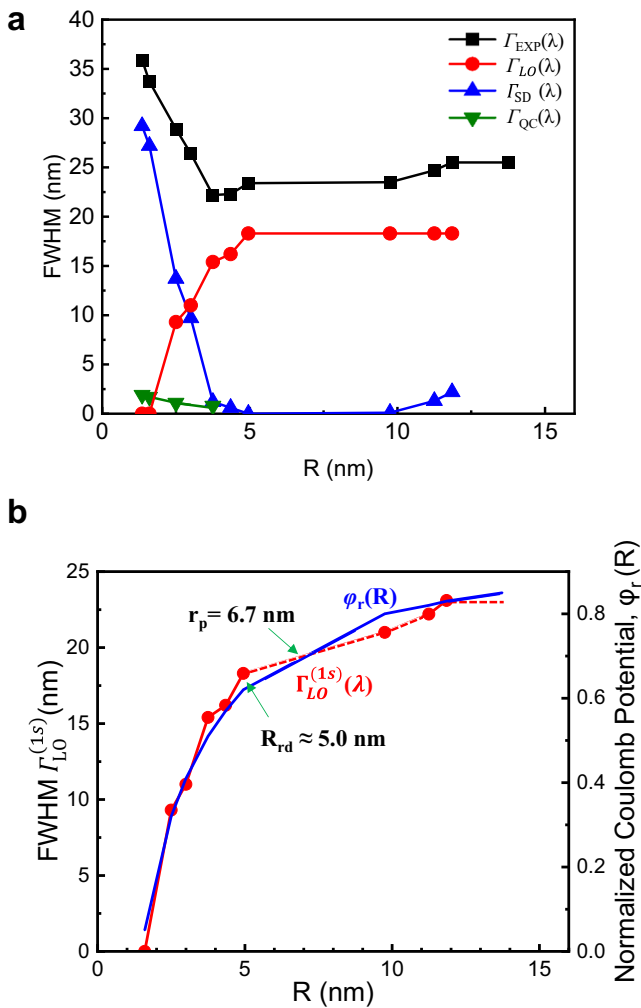
Fig. 5 Four distinct contributions to net linewidth. a Corrected four distinct contributions to the net experimental linewidth $\Gamma_{EXP}(\lambda)$ (black) of MAPbBr$_3$ vs. CNC (confined nanocrystals) radius, where $\Gamma_{LO}(\lambda)$ (red) indicates the FWHM caused by the exciton-LO phonon Fröhlich coupling, $\Gamma_{QC}(\lambda)$ (green) indicates the FWHM (full-width at half-maximum) caused by the quantum-confinement, and $\Gamma_{SD}(\lambda)$ (blue) denotes the corrected externally-introduced FWHM that is caused exclusively by the CNC-size distribution. **b** R-dependent Γ_{LO}^{ext} and the reduced long-range Coulomb potential $\varphi_r(R)$ (blue) 1over a wide range of CNC radius up to the onset R_c of the PL blue shift where the weak quantum-confinement effect begins to occur. For $R \leq 5.0$ nm, we used a red solid line to represent the size-dependent Γ_{LO} because $\Gamma_{LO}(R) = \Gamma_{LO}^{ext}$ in this size range, where $\Gamma_{LO}(R)$ is used to emphasize the strongly R-dependent corrected $\Gamma_{LO}(\lambda)$ for $R \leq 5.0$ nm in the PL-λ spectrum. On the contrary, we used a red dashed line for $R>5.0$ nm as this line represents Γ_{LO}^{ext} rather than the correct intrinsic $\Gamma_{LO}(bg)$, where $\Gamma_{LO}^{ext}(\lambda) = \Gamma_{LO}(bg) + (\Gamma_o - \Delta_R)$ for $R \geq 4.95$ nm, Herein, we adopt Γ_{LO}^{ext} values to correlate the size-dependent Γ_{LO} with $\varphi_r(R)$ because we are primarily concerned with the decaying behavior of Γ_{LO} for the CNC radius smaller than $R_{rd}(\approx 5.0$ nm). The estimated result shows that $\Gamma_{LO}^{(1s)}(\lambda)$ reduces to zero when $\phi^{LR}(R)$ [i.e., $\varphi_r(R)$] disappears at $R_p =1.6$ nm; this result suggests that the intrinsic linewidth broadening caused by the exciton-LO phonon coupling is closely correlated with the driving force for the formation of large Fröhlich polarons.

formation of large Fröhlich polarons disappears at $R_o(\sim 1.50$ nm). This prediction accords well with the computational results (Fig. 5b). Thus Eq. (8) shows that the line broadening caused by the exciton-LO phonon coupling can be linearly correlated with the

driving force for the formation of large Fröhlich-polarons which arises similarly from the electron-LO phonon coupling.

Computation of R-dependent $\varphi_r(R)$ using Eq. (7) requires use of a suitable value of the effective-action thickness L_{eff} of the surrounding low-permittivity solvent layer. Using Eq. (6) and the experimental finding that $|\phi^{LR}(R)| = 0$ at R_o, we obtain the following approximation: $L_{eff} = \frac{\varepsilon_r^s}{(\varepsilon_r^Q - 2\varepsilon_r^s)}R_o \approx 0.43R_o \approx 0.65$ nm. In obtaining this value, we adopt $\varepsilon_r^Q = 10.75$ (ref. [30]), $\varepsilon_r^s \approx 2.5$ (toluene), and $R_o = 1.5$ nm (Fig. 5b). Thus, L_{eff} to exert the dielectric-confinement effect on the MAPbBr$_3$ CNC-core is limited to a short distance (~ 0.65 nm) from the core surface.

Highly asymmetric PL spectra for $D_p<3.0$ nm. Considering the experimental observation (Fig. 3a), we adopt the following asymmetric Gaussian-like function $g(R)$ for the normalized CNC-size distribution with respect to its modal size R_p: $g(R) = \exp\{-(R - R_p)^2/(2\sigma_R^2)\}$ for $R \geq R_p$, where σ_R denotes the standard deviation in the size distribution for $R \geq R_p$. Similarly, $g(R) = \exp\{-(R - R_p)^2/(2\sigma_{R'}^2)\}$ with the standard deviation of $\sigma_{R'}$ for $R \leq Rs_p$. The ratio of these two standard deviations is simply given by the ratio of the two distinct half-widths at half-maximum in $g(R)$, i.e., $\sigma_R/\sigma_{R'} = \Delta R_{1/2}/\Delta R'_{1/2}$ (Fig. 6a, left-hand side).

We consider an empirical relation between the (modal) particle size and the PL wavelength to convert the asymmetric $g(R)$ function to the corresponding PL spectrum $f(\lambda)$. For a limited range of the particle size, the R-dependent PL λ of MAPbBr$_3$ is described by the empirical linear relation (Fig. 2b): $R = a\lambda + b$, where both R and λ have units of nanometers. Linear regression estimated $a = 0.012$ (dimensionless) in the vicinity of $D_p = 2.7$ nm (i.e., $R_p = 1.35$ nm) (Supplementary Notes 2). Using this empirical linear relation, we obtain the PL spectrum $f(\lambda)$ that corresponds to a particular CNC-size distribution, $g(R)$ for $\lambda \geq \lambda_p$:

$$f(\lambda) = \exp\left\{-a^2\left(\lambda - \lambda_p\right)^2/2\sigma_R^2\right\} = \exp\left\{-\left(\lambda - \lambda_p\right)^2/2\sigma_\lambda^2\right\},$$
(9)

where $\sigma_\lambda \equiv \sigma_R/a = 83.3\sigma_R \gg \sigma_R$. Thus, for the CNC-size distribution centered at $D_p = 2.7$nm $(R_p = 1.35$ nm), the standard deviation of the PL-λ spectrum (σ_λ) is substantially bigger than that for the asymmetric CNC-size distribution itself, σ_R (Fig. 6b, left-hand side).

The following relationship can be readily obtained from $g(R)$ and $f(\lambda)$:

$$\left(\frac{\Delta\lambda_{1/2}}{\Delta\lambda'_{1/2}}\right) = \left(\frac{\sigma_R}{\sigma_{R'}}\right) = \left(\frac{\sigma_\lambda}{\sigma_{\lambda'}}\right) = \left(\frac{\Delta R_{1/2}}{\Delta R'_{1/2}}\right) > 1. \quad (10)$$

Equation (10) is only valid for the linewidth broadening that is caused by the CNC-size distribution with $\Gamma_{SD}(\lambda) = \Delta\lambda_{1/2} + \Delta\lambda'_{1/2}$ (Fig. 6a). The exciton-LO phonon coupling contribution to the net linewidth $\Gamma_{LO}(\lambda)$ is 0 at $D_p = 2.7$ nm $(R_p = 1.35$ nm) (Fig. 5a). Thus, the experimentally-observed FWHM is primarily determined by the linewidth Γ_{SD} that is exclusively caused by the CNC-size distribution at $D_p = 2.7$ nm. Therefore, Eq. (10) explains the observed asymmetric PL-λ spectrum at $D_p = 2.7$ nm (Fig. 2a) which is skewed toward the long-λ side of the modal wavelength λ_p. This explanation is consistent with a schematic $f(\lambda)$ spectrum, which is characterized by $(\Delta\lambda_{1/2}/\Delta\lambda'_{1/2}) > 1$ (Fig. 6a).
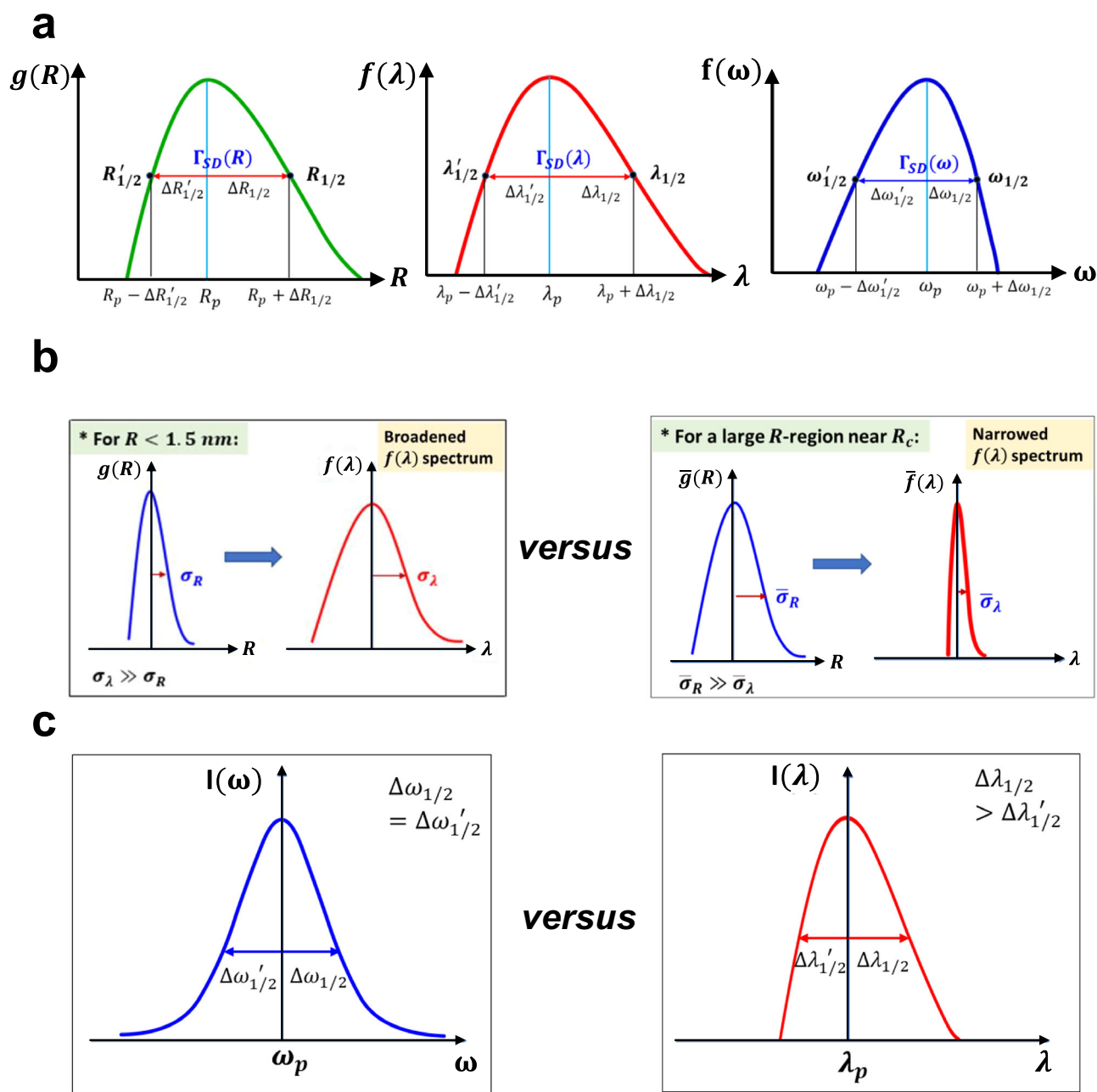
Fig. 6 CNC-size-dependent asymmetric PL spectra. a Schematic representation of the asymmetric PL-λ spectrum $f(\lambda)$ and the corresponding PL-ω spectrum $f(\omega)$ which arise solely from the asymmetric CNC-size distribution $g(R)$ for $D_p < 3.0$ nm $(= R_p < 1.5$ nm$)$. In this small-R region, all three FWHMs $\Gamma_{SD}(R), \Gamma_{SD}(\lambda)$, and $\Gamma_{SD}(\omega)$ are exclusively caused by the CNC-size distribution because $\Gamma_{LO}(\lambda) = 0$ and $\Gamma_{SD}(\lambda) \gg \Gamma_{QC}(\lambda)$ for $D_p < 3.2$ nm. **b** Size-distribution function $g(R)$ and the corresponding $f(\lambda)$ spectrum with a pronounced line broadening for $R < 1.5$ nm vs. the size-distribution function $\bar{g}(R)$ and the **c**orresponding $\bar{f}(\lambda)$ spectrum with a significant linewidth narrowing for the large-R region near R_c (the onset of the PL blue shift, 13.75 nm for MAPbBr$_3$). **c** Symmetric Lorentzian PL-ω spectrum $I(\omega)$ vs. asymmetric pseudo-Lorentzian PL-λ spectrum $I(\lambda)$ for $D_p >$ exciton Bohr diameter ($\approx$ 9 nm for MAPbBr$_3$).

Contrary to the PL-λ spectrum, the PL-ω spectrum for $D_p < 3$ nm is characterized by skew toward the low-ω side of the modal frequency ω_p (Fig. 2d). We derived $(\Delta\omega'_{1/2}/\Delta\omega_{1/2}) = (\sigma_\omega/\sigma_{\omega'}) \approx (\Delta\lambda_{1/2}/\Delta\lambda'_{1/2}) = \{(\sigma_R/a)/(\sigma'_R/a)\} > 1$, which correlates the asymmetry in the PL-ω spectrum with the asymmetry in the PL-λ spectrum or in the CNC-size distribution (Supplementary Notes 2). This relation predicts that contrary to the PL-λ spectrum, the PL-ω spectrum $f(\omega)$ should show a skew toward the low-ω side of the modal frequency ω_p (Fig. 6a). This prediction concurs with the experimental PL-ω spectrum at $D_p =$

2.7 nm (Fig. 2d), where the $\Gamma_{LO}(\lambda)$ contribution to the total FWHM is 0 (Fig. 5a). To quantify this relationship, we considered the degree of asymmetry in the PL-ω spectrum, which is defined as $\delta\omega_{1/2} = \Delta\omega'_{1/2} - \Delta\omega_{1/2} > 0$. Several algebraic rearrangements (Supplementary Notes 2) yield

$$\delta\omega_{1/2} = \Delta\omega'_{1/2} - \Delta\omega_{1/2} = \left(\frac{\Gamma_{SD}(\omega)}{\Gamma_{SD}(R)}\right)\left(\Delta R_{1/2} - \Delta R'_{1/2}\right) > 0.$$

(11)

This relation again predicts that the PL-ω spectrum is skewed toward the low-ω side of the modal frequency, and is

Table 3 Four distinct contributions to the size-dependent experimental linewidth of MAPbBr$_3$ CNCs, expressed in nm value.

D_p (nm)	R_p (nm)	λ_p (nm)	$\Gamma_{EXP}(\lambda)$ (nm)	$\Gamma_{SD}(\lambda)$ (nm)	$\Gamma_{QC}(\lambda)$ (nm)	$\Gamma_{LO}(\lambda)$ (nm)	ω_p ($\times 10^{15}$ s^{-1})	Δ_R (nm)
2.7	1.35	475	35.9	29.2	1.9	0	3.966	5.8
3.2	1.6	498	33.7	27.2	1.7	0	3.783	4.8
5.0	2.5	514	28.9	13.7	1.1	9.3	3.665	4.8
6.0	3.0	518	26.4	9.7	0.9	11.0	3.637	4.8
7.5	3.75	522	22.2	1.2	0.8	15.4	3.609	4.8
8.7	4.35	523	22.3	0.6	0.7	16.2	3.602	4.8
9.9	4.95	524	23.4	0.0	0.6	18.3	3.595	4.8
19.5	9.75	525.1	23.5	0.1	0.3	18.3	3.587	2.1
22.5	11.25	526.0	24.7	1.3	0.3	18.3	3.582	0.9
23.7	11.85	526.2	25.5	2.2	0.2	18.3	3.580	0.0
27.5	13.75 ($= R_c$)	527.0 ($= \lambda_c$)	25.5	—	—	—	3.575	—

*$\Gamma_{EXP}(\lambda)$ is equal to the sum of four contributions, $\Gamma_{LO}(\lambda)$, $\Gamma_{QC}(\lambda)$, $\Gamma_o(\lambda)$ and $\Gamma_{SD}(\lambda)$, according to Eq. (1), where $\Gamma_o(\lambda)$ is 4.8 nm which is essentially independent of the CNC size.
*It can be shown readily by comparing Eq. (3) with Eq. (17) that $\Gamma_{LO}^{ext} = \Gamma_{LO} + (\Gamma_o - \Delta_R)$. This signifies that the nominal Γ_{LO}^{ext} absorbs the Γ_o term[27] into Γ_{LO} but is corrected by the overestimate Δ_R made in the experimental extraction of Γ_{SD}^{ext}.
*For $R_p \geq 4.95$ nm, $\Gamma_{LO}(\lambda)$ is equal to $\Gamma_{LO}(bg)$ which is estimated to be 18.3 nm in the PL-λ spectrum (Methods for details).
*The CNC size-dependent Δ_R value, as displayed in the last column, was computed using the following equation: $\Delta_R = \{\Gamma_{LO} + \Gamma_{QC} + \Gamma_{SD}^{ext} + \Gamma_o\} - \Gamma_{EXP}$. This equation is obtained by combining Eq. (2) with Eq. (1).

consistent with the result shown in Fig. 2d at $D_p = 2.7$ nm. We have estimated that $\Gamma_{SD}(\omega) = \{\Gamma_{SD}(\lambda)/\Gamma_{EXP}(\lambda)\} \cdot \Gamma_{EXP}(\omega) = (29.2/35.9) \times 0.293 \times 10^{15}$ s$^{-1} = 0.238 \times 10^{15}$ s^{-1} at $D_p = 2.7$ nm (Tables 2 and 3) and found experimentally that $\Gamma_{SD}(R) \approx 1$ nm and $\Delta R_{1/2} - \Delta R'_{1/2} \approx 0.2$ nm. Using these values in Eq. (11) predicts $\delta\omega_{1/2} \approx 0.05 \times 10^{15}$ s^{-1}, which is much smaller than the modal frequency $\omega_p = 3.97 \times 10^{15}$ s^{-1} at $D_p = 2.7$ nm. Thus, $\delta\omega_{1/2}/\omega_p \approx 0.012 \ll 1$. Equation (11) shows that the degree of asymmetry in the PL-ω spectrum is determined by the degree of asymmetry in the CNC-size distribution, $(\Delta R_{1/2} - \Delta R'_{1/2})$. Equation (11) can be alternatively written as $\delta\omega_{1/2}/\Gamma_{SD}(\omega) = (\Delta R_{1/2} - \Delta R'_{1/2})/\Gamma_{SD}(R) \approx \frac{0.2}{1} = 0.2$. Thus, $\delta\omega_{1/2}$ is comparable to $\Gamma_{SD}(\omega)$; this indicates a highly asymmetric PL-ω spectrum at $D_p = 2.7$ nm. This prediction accords well with the experimental PL-ω spectrum (Fig. 2d) at $D_p = 2.7$ nm.

However, the FWHM value of the present MAPbBr$_3$ QD at $D_p = 2.7$ nm is noticeably larger than that of the MAPbBr$_3$ QD (with a similar D_p of 2.12 nm) prepared by low-temperature liquid-nitrogen passivation[38] to restrain the defects of surface Br vacancy (V_{Br}): FWHM of ~35 nm (Table 1) *vs.* FWHM < ~20 nm. Here, we refer to as a QD if the corresponding CNC radius is smaller than the exciton Bohr radius (a_B). It has been reported that these kinds of vacancy defects can be facilely generated on the surface of perovskite QDs during the fast nucleation and growth steps[39,40]. In addition, highly dynamic organic capping agents, such as *n*-alkylamine or oleic acid used in the present study, cannot stabilize the perovskite QD structure well, easily regenerating V_{Br} defects at room temperature[41,42]. Considering the restraining effects of liquid-nitrogen passivation and facile defects formation, the observed FWHM broadening of the present MAPbBr$_3$ blue-emission QD can be attributed not only to a finite CNC-size distribution but also to surface vacancy defects or poor structural stability probably due to organic capping agents.

The most prominent feature of the PL-ω or PL-λ spectrum at $D_p = 2.7$ nm is the extended skew toward the low-energy side of the modal frequency (Fig. 2d) but with a small degree of asymmetry at half-maximum ($\delta\omega_{1/2}/\omega_p \approx 0.012$). This tail-like extended skew is also observed in liquid-nitrogen passivation-treated deep-blue emission QDs[38] and suggests that emissive-band tail states with a large tail width exist just below the excited singlet $|1S_e\rangle$ state[43–45]. This type of emission from the band tail states has been reported in all-inorganic halide perovskite, CsPbBr$_3$, for ultrasmall (~ 3 nm) CNCs[45]. Photocarriers produced by the above-gap excitation can then relax into the band tail states and then recombine radiatively; the result is a long tail on the low-energy side of the PL peak[45]. Thus, the emission from the band-tail states seems to be mainly responsible for the long tail, whereas the asymmetry in the CNC-size distribution causes the asymmetric PL-ω spectrum at the half-maximum for modal size smaller than ~ 3 nm in the MAPbBr$_3$ CNC (Fig. 2d).

Asymmetric Lorentzian PL-λ spectrum for $D_p > D_B$. The estimated $\Gamma_{SD}(\lambda)$ decreases noticeably as modal size increases and reaches its minimum value at $D_p = 19.5$ nm (Fig. 5a). To explain this behavior, we consider the experimental PL-λ vs. R curve. Near R_c ($= 13.75$ nm), the R-dependent PL λ is described by an empirical linear relation: $R = a'\lambda + b'$, with estimated $a' = 3.1$ (Supplementary Notes 2). The corresponding hypothetical PL-λ spectrum solely caused by the CNC-size distribution can be written as

$$\bar{f}(\lambda) = \exp\left\{-\frac{(a')^2(\lambda - \lambda_p)^2}{2\bar{\sigma}_R^2}\right\} = \exp\left\{-\frac{(\lambda - \lambda_p)^2}{2\bar{\sigma}_\lambda^2}\right\} \quad (12)$$

where $\bar{\sigma}_\lambda = \bar{\sigma}_R/a' = \frac{\bar{\sigma}_R}{3.1}$. Thus, compared with the CNC-size distribution, a significant linewidth narrowing ($\bar{\sigma}_\lambda = \bar{\sigma}_R/3.1$) is expected in the hypothetical PL-λ spectrum near R_c. However, this is in sharp contrast with the pronounced linewidth broadening in the PL-λ spectrum for $D_p < 3.0$ nm ($R_p < 1.5$ nm), where $\sigma_\lambda = \sigma_R/a = 83.3\sigma_R$ (Fig. 6b). This prediction qualitatively accords with the estimated $\Gamma_{SD}(\lambda)$ (Table 3): at $D_p = 2.7$ nm ($R_p = 1.35$ nm), $\Gamma_{SD}(\lambda) \approx 30$ nm, whereas for $D_p \geq 19.5$ nm ($R_p \geq 9.75$ nm), $\Gamma_{SD}(\lambda) \approx 1$ nm.

MAPbBr$_3$ has D_B ($2a_B$) between 8.76 nm (≈ 9 nm)[30] and 10 nm[29,46]. According to our estimate (Fig. 5a, Table 3), the linewidth Γ_{LO} caused by the exciton-LO phonon Fröhlich coupling dominates over the externally introduced linewidth Γ_{SD} arising from the CNC-size distribution in this large-R region, where $D_p > D_B \approx 9$ nm: $\Gamma_{LO} > 16.2$ nm *vs.* $\Gamma_{SD} \approx 0.5$ nm. Thus, the net line-shape in this large-R region is determined primarily by the exciton-LO phonon coupling. Under this condition ($D_p > 9$ nm), the net line-shape is essentially governed by the

symmetric Lorentzian PL-ω spectrum $I(\omega)$[24].

$$I(\omega) = I_o \left\{ \frac{\left(\frac{\Gamma_{LO}(\omega)}{2}\right)}{(\omega_p - \omega)^2 + \left(\frac{\Gamma_{LO}(\omega)}{2}\right)^2} \right\} = I_o \left\{ \frac{\left(\frac{\gamma}{2}\right)}{(\omega_p - \omega)^2 + \left(\frac{\gamma}{2}\right)^2} \right\} \quad (13)$$

where $\Gamma_{LO}(\omega) = 2\Delta\omega_{1/2} \equiv \gamma$ and $\Delta\omega_{1/2}$ denotes the half-width at half-maximum of a given symmetric PL-ω spectrum. This prediction of the symmetric Lorentzian spectrum is consistent with the experimentally-observed PL-ω spectra for $D_p \geq 7.5$ nm (Fig. 2d).

We then calculated the line-shape of the PL-λ spectrum in this large-R region. By definition, $\omega = 2\pi c/\lambda$, where c is the speed of light, so $(\omega_p - \omega)^2 = (2\pi c)^2 \left(\frac{1}{\lambda_p} - \frac{1}{\lambda}\right)^2$; substituting the right-hand side into Eq. (13) and rearranging eventually yields an expression for the normalized PL-λ spectrum $I(\lambda)$:

$$I(\lambda) = \left(\frac{\gamma'}{2}\right) \left(\frac{\lambda}{\lambda_p}\right) \left\{ \frac{\left(\frac{\gamma'}{2}\right)}{(\lambda - \lambda_p)^2 + \left(\frac{\gamma'}{2}\right)^2} \right\} \quad (14)$$

where $\gamma' \equiv \frac{\lambda_p \lambda}{2\pi c} \gamma$. Thus, the modified linewidth $\left(\frac{\gamma'}{2}\right)$ is not constant, but depends on PL wavelength λ. $I(\lambda)$ is asymmetric with respect to λ_p (Fig. 6c), although $I(\omega)$ is symmetric Lorentzian[24] with respect to ω_p [Eq. (13)]. It can be shown that $\Delta\lambda_{1/2} > \Delta\lambda'_{1/2}$, where $\Delta\lambda_{1/2} \equiv \lambda_{1/2} - \lambda_p$ and $\Delta\lambda'_{1/2} \equiv \lambda_p - \lambda'_{1/2}$ (Fig. 6c). Thus, the asymmetric pseudo-Lorentzian PL-λ spectrum, which is mostly caused by the exciton-LO phonon coupling for $D_p > 7.5$ nm (or $> D_B$), is characterized by skew toward the long-λ side of λ_p. The PL-λ spectra (Fig. 2a) for $D_p \geq 7.5$ nm show this asymmetry. To more quantitatively assess the asymmetry, we define the degree of asymmetry in the PL-λ spectrum as $\delta\lambda_{1/2}(L) \equiv \Delta\lambda_{1/2} - \Delta\lambda'_{1/2} > 0$, where (L) is used to emphasize that the spectrum is pseudo-Lorentzian. We derived the following simple relation for the degree of asymmetry (Supplementary Notes 2):

$$\frac{\delta\lambda_{1/2}(L)}{\Gamma_{LO}(\lambda)} = \frac{\Gamma_{LO}(\omega)}{\omega_p} \ll 1, \quad (15)$$

In the above equation, $\Gamma_{LO}(\lambda)$ denotes the FWHM in the pseudo-Lorentzian PL-ω spectrum, whereas $\Gamma_{LO}(\omega)$ designates the FWHM in the corresponding Lorentzian PL-λ spectrum. For MAPbBr$_3$ CNCs at $D_p = 19.5$ nm, $\omega_p = 3.587 \times 10^{15}$ s^{-1} and $\Gamma_{LO}(\omega) = \Gamma_{LO}(\hbar\omega)/\hbar \approx 0.12 \times 10^{15}$ s^{-1}, where $\Gamma_{LO}(\hbar\omega) = hc\,\Gamma_{LO}(\lambda)/\lambda_p^2 \approx 82.3$ (meV) with $\lambda_p = 525.1$ nm and $\Gamma_{LO}(\lambda) = 18.3$ nm at $D_p = 19.5$ nm. Hence, $\delta\lambda_{1/2}(L)/\Gamma_{LO}(\lambda) = 0.033 \ll 1$. This estimate demonstrates that the degree of asymmetry $\delta\lambda_{1/2}(L)$ is much smaller than the FWHM itself [$\Gamma_{LO}(\lambda)$], and indicates that the PL-λ spectrum [Eq. (14)] is only slightly distorted pseudo-Lorentzian.

Conclusions

The use of colloidal perovskite nanocrystals (PNCs) is an effective strategy (i) to achieve color tunability by suitably adjusting the degree of PL blue shift and (ii) to increase the PLQE of MHP crystals by exploiting the quantum-confinement effect. However, the approach of colloidal PNCs inevitably introduces two additional broadening effects on the spectral linewidths, Γ_{SD} and Γ_{QC}, which possibly deteriorate the ultrahigh color purity of MHPs. The linewidth broadening due to these two factors is pronounced especially at small CNC sizes. Considering these, we develop a

simple method to extract Γ_{SD} at a given modal size by combining the experimental size-distribution histogram with the size-dependent PL-λ curve (Fig. 3b). We subsequently analyze that due to a nonlinearity in the size-dependent PL-λ curve, this extracted linewidth (Γ_{SD}^{ext}) always overestimates the correct Γ_{SD} by Δ_R [Eq. (2)]. We develop a semi-empirical method to simultaneously obtain this size-dependent overestimate Δ_R and Γ_o. Γ_{QC} as a function of the CNC size is calculated using our theoretical method. Having obtained (i) the size-dependent Γ_{SD} and Γ_{QC} and (ii) a constant contribution of Γ_o (≈ 4.8 nm), we estimate the contribution Γ_{LO} of the exciton-LO phonon Fröhlich coupling to Γ_{net} by applying Eq. (1). We further deduce that Γ_{LO} for the bulk perovskite grains is 18.3nm [Fig. 5a and Table 3]. We show that Γ_{LO} of MAPbBr$_3$ decreases as CNC size decreases and disappears at the CNC radius $R_p = 1.60$ nm [Fig. 5a]. We show that the line broadening caused by the exciton-LO phonon coupling Γ_{LO} can be linearly correlated with the driving force for the formation of large Fröhlich-polarons which arises similarly from the electron-LO phonon coupling [Fig. 5b].

Methods

Synthesis of perovskite nanocrystals. MAPbBr$_3$ NCs were fabricated using ligand-assisted reprecipitation in air at room temperature[46]. The precursor solution that contained amine ligands was prepared by dissolving 0.3 mmol of CH$_3$NH$_3$Br (Dyesol), 0.4 mmol of PbBr$_2$ (Aldrich, 99.999%) and 40 µL of n-hexylamine (Aldrich, 99%) in 10 mL of anhydrous N, N-dimethylformamide (DMF, Aldrich, 99.8%). To synthesize medium-sized particles, reagents for precursor and n-hexylamine were dissolved in 5 mL of DMF in the same molar ratio used to synthesize the NCs. Then 10% of the precursor-mixture volume was injected into 5 mL of toluene that included various concentrations of oleic acid (Aldrich, 99%; from 0.5 to 100 µL) under vigorous stirring to induce crystallization. After 10 min, the colloidal solutions were centrifuged at 3000 rpm for 10 min to precipitate large particles. The supernatant was collected, and the precipitate was discarded.

Photoluminescence and transmission electron microscopy measurements. PL spectra of PNCs were acquired using a JASCO FP8500 spectrofluorometer in colloidal dispersion states. The measurements were performed using a 150-W Xenon lamp light source and a photomultiplier tube detector with excitation wavelength of 405 nm. A highly concentrated colloidal dispersion is accompanied by a red shift in the PL spectrum owing to the photon reabsorption[47]; therefore, the PL measurement was conducted in a highly diluted dispersion that did not show any blue shift upon further dilution (Absorbance <0.5 at 405nm). Perovskite-nanoparticle colloidal dispersions were dropped onto a formvar/carbon supported copper grids right after the PL measurement. TEM measurement was conducted using a Tecnai F20 at an acceleration voltage of 200 kV.

Image cytometry analysis. The size information for each particle was extracted using image-analysis software (ImageJ 1.41n, NIH, USA) except small particles (< 5 nm) due to a low contrast ratio. The obtained bright-field optical TEM images were converted to 8-bit images after adjusting the contrast ratio and brightness. Then the areas were acquired and used to calculate the diameter. More than 400 particles were measured at each nominal size. The small particles (< 5 nm) were close to perfectly circular and uniform, so the diameter of a small particle was directly measured by marking opposite ends. For this measurement, the modal diameter, which corresponds to the peak in the size-distribution histogram, was obtained by measuring more than 200 particles in each.

Semi-empirical estimates of four distinct contributions to net linewidth. We first consider a possible discrepancy between the modal wavelength λ_p and the experimentally measured wavelength λ_{ms} for a colloid dispersion having a finite size distribution. Nine size-dependent peak values in the PL-λ spectra (Fig. 2a) thus actually represent various size-dependent λ_{ms} values (rather than λ_p values) of MAPbBr$_3$ CNCs having various modal diameters. λ_{ms} is sensitive to the nonlinearity in the PL-λ vs. CNC size curve (Fig. 2b) and consequently to the size-distribution characteristics of dispersed CNC particles. In contrast, λ_p is an intrinsic property and thus independent of the size-distribution characteristics. In the next sub-section, we will show theoretically that there exists a unique 1:1 correspondence between the particle radius (R_p) and λ_p with an increasing tendency of the PL blue shift (moves towards a shorter λ_p as R_p decreases (Figs. 1d and 2b)[46]. We will show that $\lambda_p > \lambda_{ms}$ if the PL-λ vs. CNC size curve is characterized by a nonlinear variation in λ across R_p (Fig. 1d). As shown in Fig. 2b, this nonlinear variation in λ applies to the present MAPbBr$_3$ CNCs dispersion, especially for small CNC sizes.

We examine a colloidal dispersion having symmetrical size-distribution characteristics for dispersed CNCs to show the difference between λ_p and λ_{ms}. We can show that asymmetric size-distribution does not alter our conclusion of the inequality, namely, $\lambda_p > \lambda_{ms}$. Consider a colloidal dispersion having three distinct sizes with a symmetric abundance ratio of $x : 1 : x$ for simplicity. In this case, $g(R)$ in Fig. 1a is symmetric with respect to R_p. Then, λ_{ms} of this symmetric mixture is given by following equation: $\lambda_{ms} = \frac{x \bullet \lambda_{p-\Delta} + 1 \bullet \lambda_p + x \bullet \lambda_{p+\Delta}}{(1+2x)}$, where $\lambda_{p-\Delta}$ denotes the modal wavelength that corresponds to the CNC having the radius of $R_{p-\Delta}$. Similarly, $\lambda_{p+\Delta}$ denotes the modal wavelength for the CNCs having the radius of $R_{p+\Delta}$, where Δ is a positive constant. If the PL-λ curve is characterized by a nonlinear variation in λ across R_p (Fig. 2b), then we write: $\lambda_{p-\Delta} = \lambda_p - \varepsilon$ and $\lambda_{p+\Delta} = \lambda_p + \varepsilon'$. In the case of MAPbBr$_3$ CNCs dispersion, $\varepsilon > \varepsilon'$ for $R_p \leq 5nm$ (i.e., $D_p \leq 10nm$). Substituting these two relations into the above equation for λ_{ms} yields

$$\lambda_{ms} = \lambda_p - \frac{(\varepsilon - \varepsilon')x}{(1+2x)} \equiv \lambda_p - \Delta\lambda, \qquad (16)$$

where $\Delta\lambda \equiv (\varepsilon - \varepsilon')x/(1+2x) > 0$. Thus, $\lambda_p > \lambda_{ms}$. If the PL-λ curve were linear, i.e., $\varepsilon = \varepsilon'$, then λ_{ms} would be equal to λ_p.

According to Eq. (16), the measured wavelength for a dispersion having the modal (peak) radius R_p is λ_{ms} which is smaller than λ_p by $\Delta\lambda$. Inspecting the extraction diagram for a given size distribution (e.g., Fig. 3b), we can deduce that owing to the inequality $\lambda_p > \lambda_{ms}$, the experimentally extracted FWHM $\Gamma_{SD}^{ext}(\lambda)$ which is obtained from the measuring $\lambda_{ms} - R_p$ (or $\lambda_{ms} - D_p$) curve is bigger than the correct FWHM $\Gamma_{SD}(\lambda)$ obtained by the $\lambda_p - R_p$ (or $\lambda_p - D_p$) intrinsic (theoretical) curve. Thus, we can establish: $\Gamma_{SD}^{ext}(\lambda) = \Gamma_{SD}(\lambda) + \Delta_R$ [Eq. (2)], where Δ_R is positive and size-dependent. However, we cannot predict a priori the exact value of Δ_R for a particular CNC radius. In subsequent analysis, we will semi-empirically estimate Δ_R for a wide range of the CNC radius with the help of theoretically computed $\Gamma_{QC}(\lambda)$ and show that it is pronounced for small CNC sizes with $\Delta_R \geq 4.8nm$. However, it gradually decreases with increasing radius for $R > 5nm$ and decays to zero at $R = 11.85nm$ (Fig. 4b).

Our next task is to semi-empirically deduce Γ_o and $\Gamma_{LO}(bg)$, where $\Gamma_{LO}(bg)$ denotes the correct Γ_{LO} value that corresponds to the bulk grains (18.3nm for MAPbBr$_3$). To this end, we first consider the relation between $\Gamma_{LO}^{ext}(\lambda)$ and $\Gamma_{LO}(\lambda)$. Substituting Eq. (2) into Eq. (1) yields the following relation:

$$\Gamma_{EXP} = \Gamma_{QC} + \Gamma_{SD}^{ext} + \Gamma_{LO} + (\Gamma_o - \Delta_R), \qquad (17)$$

where we omitted the notation (λ) for simplicity. Comparing Eq. (17) with Eq. (3) then yields a relation between Γ_{LO}^{ext} and Γ_{LO}: $\Gamma_{LO}^{ext} = \Gamma_{LO} + (\Gamma_o - \Delta_R)$. This signifies that Γ_{LO}^{ext} absorbs the Γ_o term[27] into Γ_{LO} but is corrected by the overestimate Δ_R made in the experimental extraction of Γ_{SD}^{ext}. Let us consider a sufficiently large particle in which Δ_R is completely negligible ($R \geq 11.85nm$). This is because the PL wavelength shows a linear variation with the CNC size for $R \geq 10nm$. We have: $\Gamma_{EXP}(\lambda) = 25.5nm$, $\Gamma_{SD}^{ext}(\lambda) = \Gamma_{SD}(\lambda) = 2.2nm$, $\Delta_R = 0nm$, and the calculated $\Gamma_{QC} = 0.2nm$ at $R = 11.85nm$ (Table 3). Substituting these values into Eq. (17) yields the following simple relation:

$$\Gamma_{LO} + \Gamma_o = \Gamma_{LO}(bg) + \Gamma_o = 23.1nm(PL - \lambda) = 103meV(PL - \omega), \qquad (18)$$

where $\Gamma_{LO}(bg)$ denotes Γ_{LO} value for the bulk grains. This value (23.1nm) nearly coincides with 23.4nm(100.3meV) of the previous report[27] in which $\Gamma_{LO}(bg) + \Gamma_o$ was obtained by curve fitting of the temperature-dependent linewidth data with the Bose-Einstein distribution function. In Eq. (18), we replace Γ_{LO} with $\Gamma_{LO}(bg)$ because (i) our $(\Gamma_{LO} + \Gamma_o)$ value of 23.1nm(103meV) is nearly equal to that of a bulk polycrystalline film[27] and (ii) Γ_{LO} for $R \geq 4.95nm$ has a size-independent constant value of 18.3nm (Table 3).

Let us consider the $(\Gamma_o - \Delta_R)$-term appears in Eq. (17) for small CNC sizes. $\Gamma_{EXP}(\lambda) = 33.7nm$, $\Gamma_{SD}^{ext}(\lambda) = 32.0nm$, $\Gamma_{LO} = 0nm$ and the calculated $\Gamma_{QC} = 1.7nm$ at $R = 1.60nm$ (Tables 1 and 3). Substituting these values into Eq. (17) yields: $(\Gamma_o - \Delta_R) = 0$ at $R = 1.60nm$. Similarly, $\Gamma_{EXP}(\lambda) = 28.9nm$, $\Gamma_{SD}^{ext}(\lambda) = 18.5nm$, $\Gamma_{LO} = 9.3nm$ and the calculated $\Gamma_{QC} = 1.1nm$ at $R = 2.50nm$. These values also yield $(\Gamma_o - \Delta_R) = 0$ at $R = 2.50nm$. We can show semi-empirically that $(\Gamma_o - \Delta_R) = 0$ until R increases to 4.95nm. Therefore, $\Gamma_{LO}^{ext} = \Gamma_{LO} + (\Gamma_o - \Delta_R) = \Gamma_{LO}$ for small CNC sizes, namely, $1.60nm \leq R \leq 4.95nm$.

We are now in a position to deduce the value of Γ_o by comparing $\Gamma_{LO}^{ext}(R = 11.85nm)$ with $\Gamma_{LO}^{ext}(R = 4.95nm)$, where $\Gamma_{LO}^{ext}(R = 11.85nm)$ denotes the value of Γ_{LO}^{ext} at $R = 11.85nm$. We can write the following equation for the difference in Γ_{LO}^{ext} between these two sizes by applying the previously deduced relation that $\Gamma_{LO}^{ext} = \Gamma_{LO} + (\Gamma_o - \Delta_R)$:

$$\begin{aligned}\Gamma_{LO}^{ext}(R = 11.85nm) - \Gamma_{LO}^{ext}(R = 4.95nm) &= 23.1nm - 18.3nm \\ &= \{\Gamma_{LO}(R = 11.85nm) + \Gamma_o\} - \Gamma_{LO}(R = 4.95nm) \\ &= \{\Gamma_{LO}(bg) - \Gamma_{LO}(bg)\} + \Gamma_o = \Gamma_o,\end{aligned} \qquad (19)$$

where numerical values in the 2nd term is taken from Table 1. We use the following facts in simplifying the 3rd term: (i) $\Delta_R = 0$ at $R = 11.85nm$, (ii) $(\Gamma_o - \Delta_R) = 0$ at $R = 4.95nm$, as discussed previously. In obtaining the 4th term, we exploit the following equality: $\Gamma_{LO}(R = 11.85nm) = \Gamma_{LO}(R = 4.95nm) = \Gamma_{LO}(bg)$. This is because Γ_{LO} for $R \geq 4.95nm$ has a size-independent constant value of $\Gamma_{LO}(bg)(= 18.3nm)$ (Table 3). Thus, we finally deduce that $\Gamma_o = (23.1 - 18.3)nm = 4.8nm$ from Eq. (19). Plugging this value into Eq. (18) yields that $\Gamma_{LO}(bg) = 18.3nm$ which coincides with the deduced Γ_{LO} value for $R \geq 4.95nm$ (Table 3). Thus, we establish the following relation: $\Gamma_{LO}^{ext}(\lambda) = \Gamma_{LO}(bg) + (\Gamma_o - \Delta_R) = 18.3nm + (\Gamma_o - \Delta_R)$ for $R \geq 4.95nm$. The previous deduction that $(\Gamma_o - \Delta_R) = 0$ indicates that Δ_R

is effectively constant and is equal to 4.8nm for $1.60\text{nm} \leq R \leq 4.95\text{nm}$ (Fig. 4b).

It is expected that Δ_R decays to zero as the CNC size increases because the PL wavelength shows a linear variation with the CNC size for $D \geq 20\text{nm}(R \geq 10\text{nm})$ (Fig. 2b). We can compute this decaying Δ_R for large CNC particles by using the following obvious relation that can be obtained by combining Eq. (2) with Eq. (1) and rearranging: $\Delta_R = \{\Gamma_{\text{LO}}(bg) + \Gamma_{\text{QC}}(\lambda) + \Gamma_{\text{SD}}^{\text{ext}}(\lambda) + \Gamma_{\text{o}}(\lambda)\} - \Gamma_{\text{EXP}}(\lambda)$. Here, we replaced $\Gamma_{\text{LO}}(\lambda)$ with $\Gamma_{\text{LO}}(bg)$ having a constant value of 18.3nm for $R \geq 4.95\text{nm}$. $\Gamma_{\text{EXP}}(\lambda) = 23.5\text{nm}, \Gamma_{\text{SD}}^{\text{ext}}(\lambda) = 2.2\text{nm}, \Gamma_{\text{o}} = 4.8\text{nm}$ and the calculated $\Gamma_{\text{QC}} = 0.3\text{nm}$ at $R = 9.75\text{nm}$ (Table 1). We obtain $\Delta_R = 2.1\text{nm}$ (Table 3) using these values. Similarly, $\Gamma_{\text{EXP}}(\lambda) = 24.7\text{nm}, \Gamma_{\text{SD}}^{\text{ext}}(\lambda) = 2.2\text{nm}, \Gamma_{\text{o}} = 4.8\text{nm}$ and the calculated $\Gamma_{\text{QC}} = 0.3\text{nm}$ at $R = 11.25\text{nm}$ (Table 1). We obtain $\Delta_R = 0.9\text{nm}$ (Table 3) using these values. Finally, $\Gamma_{\text{EXP}}(\lambda) = 25.5\text{nm}, \Gamma_{\text{SD}}^{\text{ext}}(\lambda) = 2.2\text{nm}, \Gamma_{\text{o}} = 4.8\text{nm}$ and the calculated $\Gamma_{\text{QC}} = 0.2\text{nm}$ at $R = 11.85\text{nm}$ (Table 2). We obtain $\Delta_R = 0\text{nm}$ (Table 3) using these values. This prediction that $\Delta_R = 0\text{nm}$ at $R = 11.85\text{nm}$ accords well with our prediction used previously. The calculated size-dependent Δ_R is displayed in Fig. 4b. Δ_R effectively shows a constant plateau behavior up to $R = 4.95\text{nm}$ and gradually decreases with increasing radius beyond this size, effectively becoming 0 at $R = 11.85\text{nm}$. Thus, $\Gamma_{\text{SD}}^{\text{ext}}(\lambda) \approx \Gamma_{\text{SD}}(\lambda)$ for $R \geq 11.85\text{nm}$.

Nonlinear variation in the degree of PL blue shift with the CNC size. In this section, we will examine the observation that the PL wavelength decreases as the CNC size decreases (Fig. 2b), which is known as the PL blue shift. We will show theoretically that the degree of PL blue shift ($\Delta\lambda$) with decreasing radius is not linear (i.e., $\partial\Delta\lambda/\partial R \neq constant$) but is highly nonlinear. This nonlinear variation of the PL wavelength is primarily responsible for a non-zero Δ_R. To this end, we first consider the total energy of exciton [$E_{\text{exc}}(R;\alpha)$] in a CNC having radius R. It can be written as[29,48]

$$E_{\text{exc}}(R;\alpha) = E_{\text{g(b)}} + \Delta E_{\text{g}}(R;\alpha) = E_{\text{g(b)}} + \frac{\hbar^2}{2\mu_o}\left\{\frac{\pi^2}{R^2} + \left(\frac{1}{\alpha}\right)^2\right\} - \frac{e^2}{4\pi\varepsilon_o\varepsilon_r^Q}\left\{\frac{C_1'}{R} + \frac{C_2}{\alpha}\right\},$$
(20)

where $E_{\text{g(b)}}$ denotes the bulk band-gap energy, μ_o is the effective reduced mass of exciton, ε_r^Q designates the dielectric constant of a CNC (or QD) core, and $C_2 = 0.498$. The Coulomb interaction coefficient (C_1') can be viewed as the effective Madelung constant[29] for a sphere having radius R. Equation (20) is the most elaborate expression of the net exciton energy above the bulk band gap [$\Delta E_{\text{g}}(R;\alpha)$], which considers the internal relative motion between the electron and hole in a given exciton by introducing the quantum mechanical e-h correlation term, α,(ref. [48]). We consider the size-dependent PL frequency or wavelength as the next step. The total energy of exciton and the bulk band-gap energy under the condition of PL emission can be respectively written as

$$E_{\text{exc}}(R;\alpha) = \hbar\omega = hc/\lambda \text{ and } E_{\text{g(b)}} = \hbar\omega_c = hc/\lambda_{\text{c}},$$
(21)

where λ_{c} denotes the wavelength that corresponds to the onset of PL blue shift (527.0nm for MAPbBr$_3$; Tables 1 or 3). In Eq. (21), $E_{\text{g(b)}} = hc/\lambda_{\text{c}}$ represents that the PL emission from the conduction band minimum to the valence band maximum occurs with the characteristic wavelength λ_{c}. Let us now define the degree of

PL blue shift in terms of the PL wavelength.

$$\Delta\lambda \equiv \lambda_{\text{c}} - \lambda = \frac{\lambda_{\text{c}}\Delta\omega}{2\pi c} > 0,$$
(22)

where $\Delta\omega \equiv \omega - \omega_c > 0$. Combining Eqs. (21) and (22) with Eq. (20) yields the following expression:

$$\Delta\lambda = \frac{\hbar\lambda\lambda_{\text{c}}}{4\pi c\mu_o}\left\{\left(\frac{\pi^2}{R^2} + \left(\frac{1}{\alpha}\right)^2\right) - \frac{2}{a_{\text{B}}}\left(\frac{C_1'}{R} + \frac{C_2}{\alpha}\right)\right\},$$
(23)

where a_B designates the exciton Bohr radius which is defined by the following equation[49]:

$$a_{\text{B}} = \frac{4\pi\varepsilon_o\varepsilon_r\hbar^2}{\mu_o e^2} = \varepsilon_r\left(\frac{m_o}{\mu_o}\right)a_{\text{o}},$$
(24)

where m_o is the free-electron mass (9.109×10^{-31} kg), $\varepsilon_{\text{r}} = \varepsilon_{\text{r}}^Q$, and a_o denotes the Bohr radius for the ground-state 1s orbital of a hydrogen atom ($= 4\pi\varepsilon_o\hbar^2/m_o e^2 = 0.0529\text{nm}$).

We compared the quantum e-h correlation term [$(1/\alpha^2) - (2C_2/a_{\text{B}}\alpha)$] with the classical energy term [$(\pi^2/R^2) - (2C_1'/a_{\text{B}}R)$] to find a possibility of further simplification. For this purpose, we adopted the following semi-empirical correlation between α and R (ref. [29]): $\alpha = -0.27R + 2.0a_{\text{B}}$ for $R < 2.3a_{\text{B}}$. Since a_{B} of MAPbBr$_3$ is $\sim 5.0\text{nm}$ (refs. [29,46]), this linear correlation is valid for $R < 11.5\text{nm}$. Let us examine the attractive quantum e-h correlation term at $R = 4.95\text{nm}$, where a rapid increase in the degree of PL blue shift (i.e., $\Delta\lambda = \lambda_{\text{c}} - \lambda$) is observed (Fig. 2b). Thus, $(1/\alpha^2) = 1/(-0.27R + 2a_{\text{B}})^2 = +0.0133\text{nm}^{-2}$ and $(2C_2/a_{\text{B}}\alpha) = 2C_2/\{a_{\text{B}} \times (-0.27R + 10.0)\} = +0.0230\text{nm}^{-2}$. This leads to $(1/\alpha^2) - (2C_2/a_{\text{B}}\alpha) = -0.0097\text{nm}^{-2}$ at $R = 4.95\text{nm}$. On the other hand, the net repulsive classical energy term is $(\pi^2/R^2) - (2C_1'/a_{\text{B}}R) = \{(9.870/24.503) - (2 \times 1.39/5.0 \times 4.95)\} = +0.2905\text{nm}^{-2}$, where 1.39 is used for the C_1' value[29]. Thus, the classical energy term is 30 times bigger than the e-h correlation term in their magnitudes at $R = 4.95\text{nm}$. Considering this, we write the following approximation in the vicinity of $R = 4.95\text{nm}$, where a rapid change in the degree of PL blue shift ($\Delta\lambda$) is observed (Fig. 2b).

$$\Delta\lambda \approx \frac{\hbar\lambda\lambda_{\text{c}}}{4\pi c\mu_o}\left\{\frac{\pi^2}{R^2} - \frac{2C_1'}{a_{\text{B}}R}\right\} > 0$$
(25)

Equation (25) predicts that the degree of PL blue shift is inversely proportional to R^2, indicating a very rapid nonlinear increase in $\Delta\lambda(= \lambda_{\text{c}} - \lambda)$ with decreasing radius. The nonlinearity in $\Delta\lambda$ can be shown more clearly by taking partial differentiation:

$$\left(\frac{\partial\Delta\lambda}{\partial R}\right)_\alpha \approx -\frac{\hbar\lambda\lambda_{\text{c}}}{2\pi c\mu_o R^2}\left\{\frac{\pi^2}{R} - \frac{C_1'}{a_{\text{B}}}\right\} < 0$$
(26)

Here, we are concerned with the variation of $\Delta\lambda$ for $R \leq R_c(= 13.75\text{nm})$. Thus, the value inside the parenthesis (η) of Eq. (26) is always positive: $\eta > \{(9.87/13.75) - (1.39/5.0)\}\text{nm}^{-1} = 0.43\text{nm}^{-1}$. Equation (26) shows that $(\partial\Delta\lambda/\partial R)_\alpha$ is not constant but its magnitude increases very rapidly with decreasing radius.

Finally, we will show that there exists a unique 1:1 correspondence between the modal CNC size R_{p} (or D_{p}) and the modal wavelength λ_{p}, where λ_{p} actually denotes a particular wavelength (λ_{p}) that corresponds to the peak in the PL-λ spectrum: e.g., $\lambda_{\text{p}} = 524.0$ nm for $R_{\text{p}} = 4.95$ nm (Table 1). We can directly obtain the following relation that shows a unique 1:1

correspondence between λ_p and R_p from Eq. (23):

$$\lambda_p = \frac{\lambda_c}{\left[1 + \frac{\hbar \lambda_c}{4\pi c \, \mu_o}\left\{\left(\frac{\pi^2}{R_p^2} + \left(\frac{1}{\alpha_p}\right)^2\right) - \frac{2}{a_B}\left(\frac{C_1'}{R_p} + \frac{C_2}{\alpha_p}\right)\right\}\right]} \quad (27)$$

where the quantum *e-h* correlation parameter at R_p is denoted by α_p. As discussed previously, it is given by the following semi-empirical relation for $R_p < 2.3a_B$ (ref. [29]): $\alpha_p = -0.27R_p + 2.0a_B$. This semi-empirical correlation indicates that the denominator of Eq. (27) is a functional of R_p. Thus, there exists a unique 1:1 correspondence between λ_p and R_p.

Data availability

The source data and related supporting information are available from the authors on reasonable request.

References

1. Kim, Y.-H., Cho, H. & Lee, T.-W. Metal halide perovskite light emitters. *Proc. Natl. Acad. Sci. USA* **113**, 11694–11702 (2016).
2. Tan, Z. K. et al. Bright light-emitting diodes based on organometal halide perovskite. *Nat. Nanotechnol.* **9**, 687–692 (2014).
3. Schmidt, L. C. et al. Non-template synthesis of CH3NH3PbBr3 perovskite nanoparticles. *J. Am. Chem. Soc.* **136**, 850–853 (2014).
4. Kim, Y.-H. et al. Multicolored organic/inorganic hybrid perovskite light-emitting diodes. *Adv. Mater.* **27**, 1248–1254 (2015).
5. Cho, H. et al. Overcoming the electroluminescence efficiency limitations of perovskite light-emitting diodes. *Science* **350**, 1222–1225 (2015).
6. Kim, Y.-H., Kim, J. S. & Lee, T.-W. Strategies to improve luminescence efficiency of metal-halide perovskites and light-emitting diodes. *Adv. Mater.* **31**, 1–28 (2019).
7. Liu, Z. et al. Perovskite light-emitting diodes with EQE exceeding 28% through a synergetic dual-additive strategy for defect passivation and nanostructure regulation. *Adv. Mater.* **33**, 1–9 (2021).
8. Weidman, M. C., Goodman, A. J. & Tisdale, W. A. Colloidal halide perovskite nanoplatelets: an exciting new class of semiconductor nanomaterials. *Chem. Mater.* **29**, 5019–5030 (2017).
9. Kovalenko, M. V., Protesescu, L. & Bodnarchuk, M. I. Properties and potential optoelectronic applications of lead halide perovskite nanocrystals. *Science* **358**, 745–750 (2017).
10. Krieg, F. et al. Colloidal CsPbX3 (X = Cl, Br, I) nanocrystals 2.0: zwitterionic capping ligands for improved durability and stability. *ACS Energy Lett.* **3**, 641–646 (2018).
11. Park, J., Jang, H. M., Kim, S., Cho, S. H. & Lee, T.-W. Electroluminescence of perovskite nanocrystals with ligand engineering. *Trends Chem.* **2**, 837–849 (2020).
12. Zheng, K. et al. Exciton binding energy and the nature of emissive states in organometal halide perovskites. *J. Phys. Chem. Lett.* **6**, 2969–2975 (2015).
13. Jang, H. M., Kim, J.-S., Heo, J.-M. & Lee, T.-W. Enhancing photoluminescence quantum efficiency of metal halide perovskites by examining luminescence-limiting factors. *APL Mater* **8**, 020904 (2020).
14. Protesescu, L. et al. Nanocrystals of cesium lead halide perovskites (CsPbX3, X = Cl, Br, and I): novel optoelectronic materials showing bright emission with wide color gamut. *Nano Lett.* **15**, 3692 (2015).
15. Veldhuis, S. A. et al. Perovskite materials for light-emitting diodes and lasers. *Adv. Mater.* **28**, 6804–6834 (2016).
16. Droseros, N. et al. Origin of the enhanced photoluminescence quantum yield in MAPbBr3 perovskite with reduced crystal size. *ACS Energy Lett.* **3**, 1458–1466 (2018).
17. Kim, Y.-H. et al. Comprehensive defect suppression in perovskite nanocrystals for high-efficiency light-emitting diodes. *Nat. Photonics* **15**, 148–155 (2021).
18. Huang, H. et al. Growth mechanism of strongly emitting CH3NH3PbBr3 perovskite nanocrystals with a tunable bandgap. *Nature Commun.* **8**, 996 (2017).
19. Kim, Y.-H. et al. Charge carrier recombination and ion migration in metal-halide perovskite nanoparticle films for efficient light-emitting diodes. *Nano Energy* **52**, 329–335 (2018).
20. Yang, Z. et al. Spray-coated CsPbBr3 quantum dot films for perovskite photodiodes. *ACS Appl. Mater. Interfaces* **10**, 26387–26395 (2018).
21. Deng, W. et al. Organometal halide perovskite quantum dot light-emitting diodes. *Adv. Funct. Mater.* **26**, 4797–4802 (2016).
22. Dai, S. W. et al. Perovskite quantum dots with near unity solution and neat-film photoluminescent quantum yield by novel spray synthesis. *Adv. Mater.* **30**, 1870048 (2018).
23. Zhou, H. et al. Water passivation of perovskite nanocrystals enables air-stable intrinsically stretchable color-conversion layers for stretchable displays. *Adv. Mater.* **32**, 1–8 (2020).
24. Rudin, S., Reinecke, T. L. & Segall, B. Temperature-dependent exciton linewidths in semi-conductors. *Phys. Rev. B* **42**, 11218–11231 (1990).
25. Nomura, S. & Kobayashi, T. Exciton-LO phonon couplings in spherical semiconductor micro-crystallites. *Phys. Rev. B* **45**, 1305–1316 (1992).
26. Lee, J., Koteles, E. S. & Vassell, M. O. Luminescence linewidths of excitons in GaAs quantum wells below 150 K. *Phys. Rev. B* **33**, 5512–5516 (1986).
27. Wright, A. D. et al. Electron-phonon coupling in hybrid lead halide perovskites. *Nature Commun.* **7**, 11755 (2016).
28. Herz, L. M. Charge-carrier mobilities in metal halide perovskites: fundamental mechanisms and limits. *ACS Energy Lett.* **2**, 1539–1548 (2017).
29. Jang, H. M., Park, J., Kim, S. & Lee, T.-W. Quantum-confinement effect on the linewidth broadening of metal halide perovskite-based quantum dots. *J. Phys. Condens. Matter* **33**, 355702 (2021).
30. Tilchin, J. et al. Hydrogen-like Wannier-Mott excitons in single crystal of methylammonium lead bromide perovskite. *ACS Nano* **10**, 6363–6371 (2016).
31. Takagahara, T. Effects of dielectric confinement and electron-hole exchange interaction on excitonic states in semiconductor quantum dots. *Phys. Rev. B* **47**, 4569–4584 (1993).
32. Ning, J. Q., Zheng, C. C., Zhang, X. H. & Xu, S. J. Strong quantum confinement effect and reduced Fröhlich exciton-phonon coupling in ZnO quantum dots embedded inside a SiO2 matrix. *Nanoscale* **7**, 17482–17487 (2015).
33. Peters, F. M. & Devreese, J. T. Radius, self-induced potential, and number of virtual optical phonons of a polaron. *Phys. Rev. B* **31**, 4890–4899 (1985).
34. Zhu, X.-Y. & Podzorov, V. Charge carriers in hybrid organic-inorganic lead halide perovskites might be protected as large polarons. *J. Phys. Chem. Lett.* **6**, 4758–4761 (2015).
35. Devreese, J. T. & Peters, F. M. *Polarons and Excitons in Polar Semiconductors and Ionic Crystals* (Plenum Press, New York, 1984).
36. Sendner, M. et al. Optical phonons in methylammonium lead halide perovskites and implications for charge transport. *Mater. Horiz.* **3**, 613–620 (2016).
37. Devreese, J. T. *Polarons, Encyclopedia of Applied Physics* (Wiley-VCH Publishers), Vol. 14, pp. 383–409 (1996).
38. Peng, X. et al. Liquid nitrogen passivation for deep-blue perovskite quantum dots with nearly unit quantum yield. *J. Phys. Chem. C* **126**, 1017–1025 (2022).
39. Lamer, V. K. & Dinegar, R. H. Theory, production, and mechanism of formation of monodispersed hydrosols. *J. Am. Chem. Soc.* **72**, 4847–4854 (1950).
40. Wang, K. & Reeber, R. R. Thermal defects and thermal expansion of ionic crystals at high temperatures. *Phys. Status Solidi A* **146**, 621–627 (1994).
41. Pan, J. et al. Highly efficient perovskite-quantum-dot light-emitting diodes by surface engineering. *Adv. Mater.* **28**, 8718–8725 (2016).
42. Zhang, B. B. et al. General mild reaction creates highly luminescent organic-ligand-lacking halide perovskite nanocrystals for efficient light-emitting diodes. *J. Am. Chem. Soc.* **141**, 15423–15432 (2019).
43. Gourdon, C. & Lavallard, P. Exciton transfer between localized states in CdS1−xSex alloys. *Phys. Status Solidi B* **153**, 641–652 (1989).
44. He, H. P. et al. Exciton localization in solution-processed organolead trihalide perovskites. *Nat. Commun.* **7**, 10896 (2016).
45. Li, J., Gan, L., Fang, Z., He, H. & Ye, Z. Bright tail states in blue-emitting ultrasmall perovskite quantum dots. *J. Phys. Chem. Lett.* **8**, 6002–6008 (2017).
46. Kim, Y. H. et al. Highly efficient light-emitting diodes of colloidal metal-halide perovskite nanocrystals beyond quantum size. *ACS Nano* **11**, 6586–6593 (2017).
47. Zhang, W., Dai, D., Chen, X., Guo, X. & Fan, J. Red shift in the photoluminescence of colloidal carbon quantum dots induced by photon reabsorption. *Appl. Phys. Lett.* **104**, 091902 (2014).
48. Kayanuma, Y. Wannier exciton in microcrystals. *Solid State Commun.* **59**, 405–408 (1986).
49. Kayanuma, Y. Quantum-size effects of interacting electrons and holes in semiconductor microcrystals with spherical shape. *Phys. Rev. B* **38**, 9797–9805 (1988).

Author contributions

H.M.J. and T.-W.L. conceptualized the study. S.H.L. and K.Y.J. designed the experiments, performed measurements, and analyzed data. K.Y.J. and J.P. gave guidance on nano-particles synthesis and PL measurements. H.M.J. did theoretical works. All authors regularly reviewed and discussed the research. T.-W.L. supervised the experimental part of the study. H.M.J., S.H.L., K.Y.J., and T.-W.L. co-wrote the manuscript.

Competing interests

The authors declare no competing interests.

Additional information

Supplementary information The online version contains supplementary material available at https://doi.org/10.1038/s42005-023-01459-8.

Correspondence and requests for materials should be addressed to Hyun Myung Jang or Tae-Woo Lee.

Peer review information *Communications Physics* thanks Adam Wright and the other, anonymous, reviewer(s) for their contribution to the peer review of this work.

Reprints and permission information is available at http://www.nature.com/reprints

Publisher's note Springer Nature remains neutral with regard to jurisdictional claims in published maps and institutional affiliations.